

Introduction of RSPACE code

Tomoya Ono (Grad. Schl. Eng., Osaka Univ.)

Yoshiyuki Egami (Fac. Eng., Nagasaki Univ.)

Contents

1. Electronic Structure and Transport Calculation using Real-Space Finite-Difference Method

- (1) Real-Space Finite-Difference Method
- (2) Double-Grid Technique
- (3) Overbridging Boundary-Matching Method

2. Applications

- (1) Conduction property of sodium nanowire
- (2) Conduction property of aluminum nanowire
- (3) Leakage current through gate dioxide
- (4) Conduction property of C_{20} nanowires
- (5) Conduction property of C_{60} nanowires
- (6) Conduction property of helical gold nanowires
- (7) Tunnel current in STM system

Real-space finite-difference (RSFD) method

The grand-state electronic structure is obtained by solving the Schrödinger (Kohn-Sham) equation

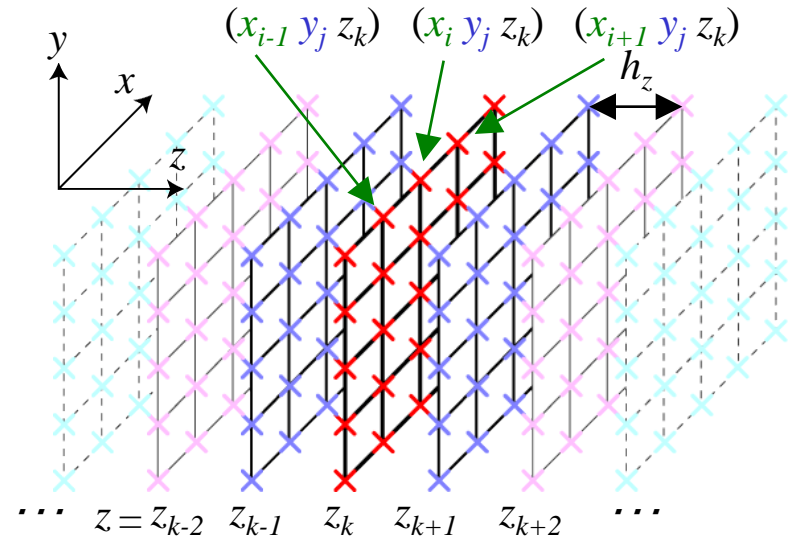
$$\left(-\frac{1}{2}\nabla^2 + V(r)\right)\psi_i(r) = \varepsilon_i\psi_i(r)$$

The RSFD method is:

- the space is divided into equal-spacing grid points,
- the wave function and potential are defined at the grid points,
- the kinetic operator is approximated to a finite-difference formula, e.g.,

$$-\frac{1}{2}\frac{d^2}{dz^2}\psi(z_k) \approx -\frac{\psi_{k+1} - 2\psi_k + \psi_{k-1}}{2h_z^2}$$

- no use of a basis-function set



Wave function ψ_{ijk} is defined at grid point (x_i, y_j, z_k)

References of the RSFD approach, .e.g.,

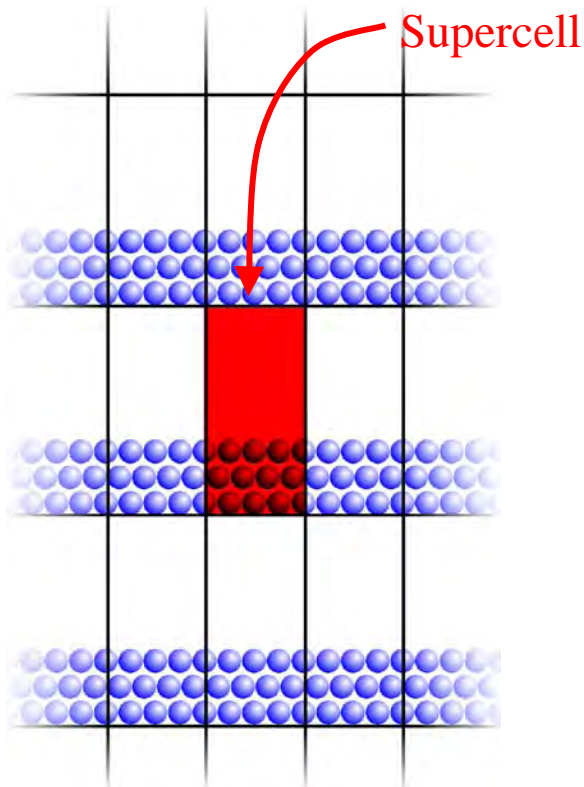
- J. R. Chelikowsky *et al.*, Phys. Rev. B **50**, 11355 (1994),
T. Ono & K. Hirose, Phys. Rev. Lett. **82**, 5016 (1999),
T. Ono & K. Hirose, Phys. Rev. B **64**, 085105 (2001),
T. Ono & K. Hirose, Phys. Rev. B **72**, 085105 (2005),
T. Ono & K. Hirose, Phys. Rev. B **72**, 085115 (2005).

Advantages of RSFD (1)

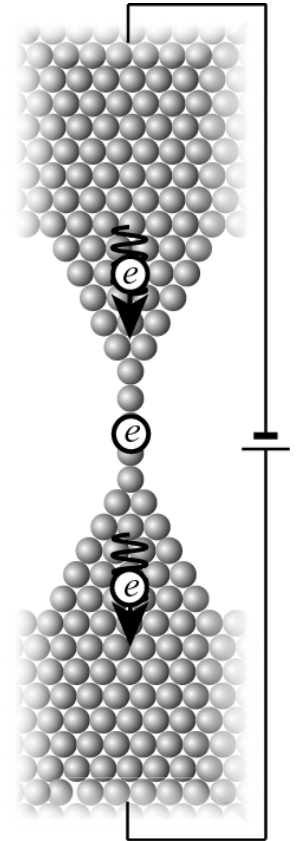
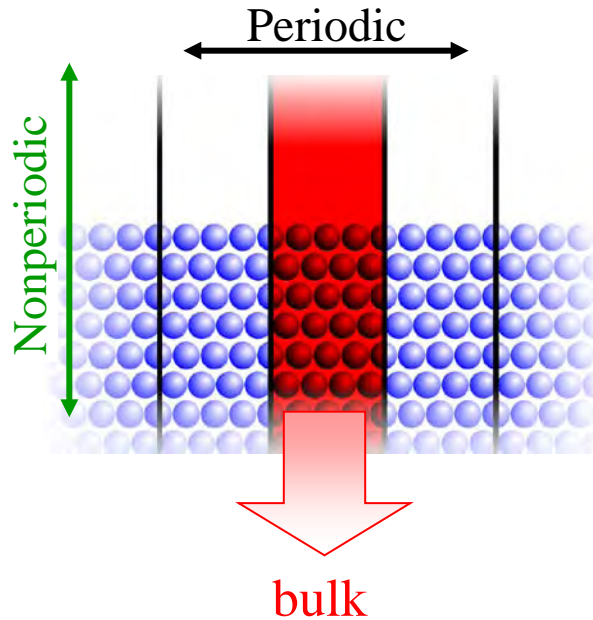
Arbitrary boundary condition is available.

Conventional plane-wave method

Repeated slab model



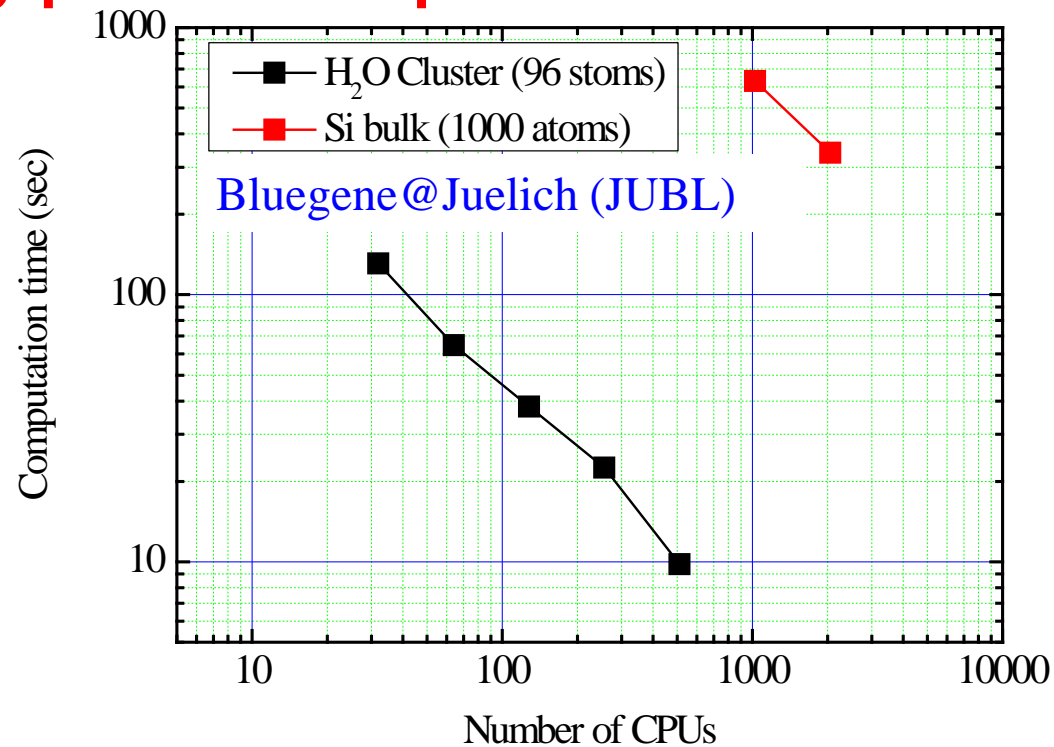
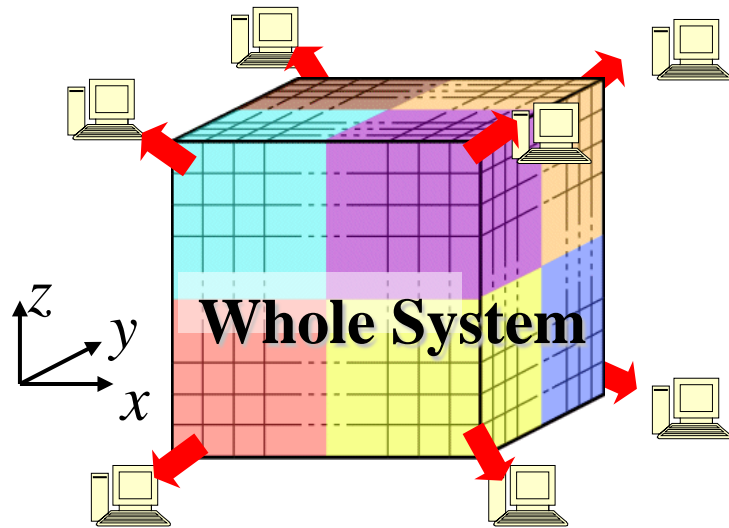
RSFD method



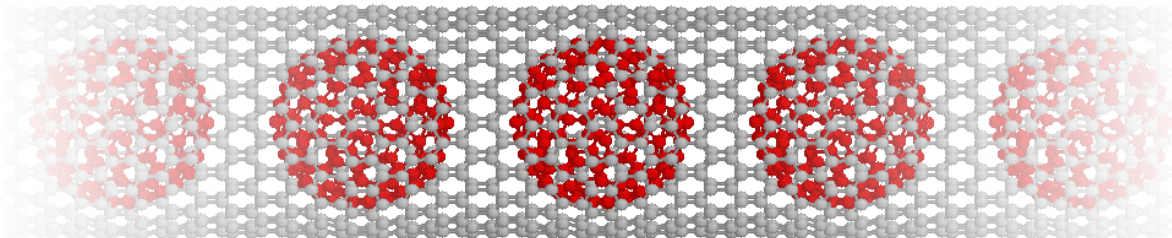
The boundary condition infinitely continuing to bulk is available.

Advantages of RSFD (2)

Advantageous on massively parallel computers.



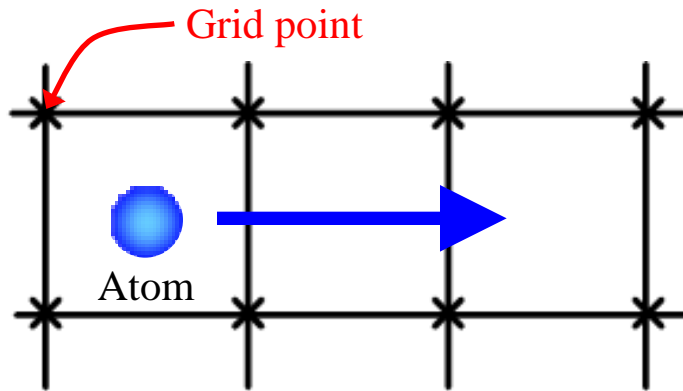
Example: Peapod C₁₈₀@(20,0)CNT (500 C atoms/supercell)



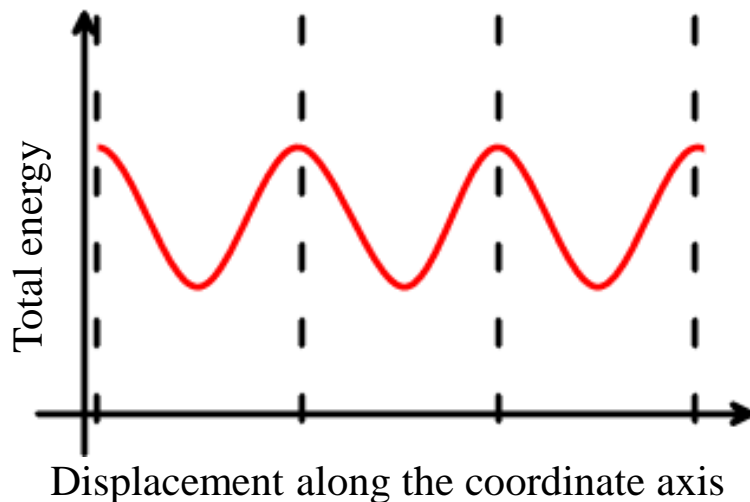
Computed by
2048CPUs of JUBL

ϕ_{CNT} : +4% ϕ_{C180} : -6% (lateral), +1% (longitudinal)
by encapsulating fullerene.

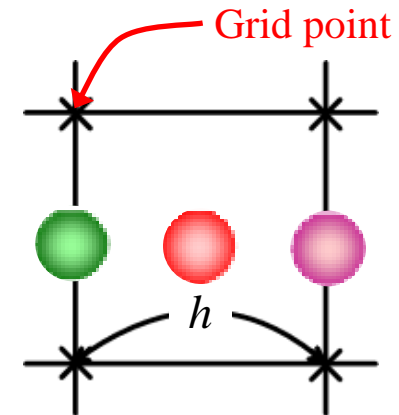
Egg box effect



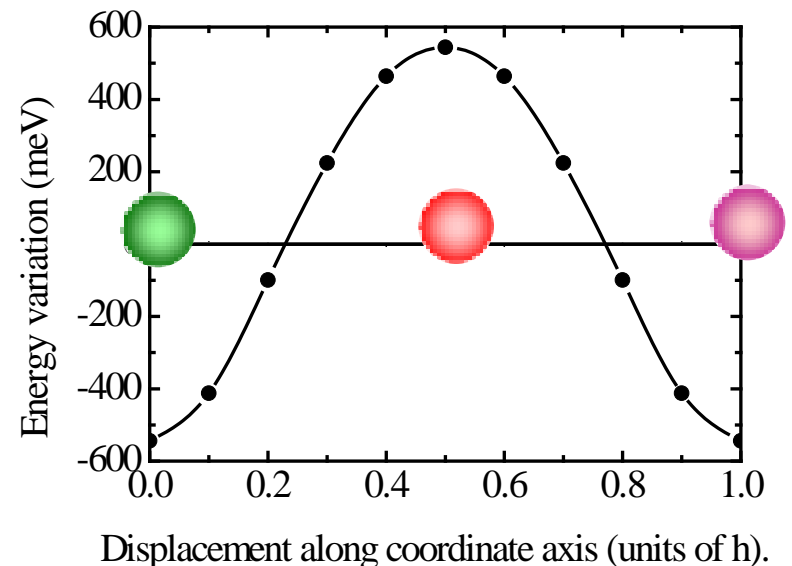
As atom is displaced relative to the grid along a coordinate axis, total energy shows **absurd dependence on the position of the atom.**



Example the case of oxygen atom



Oxygen atom is displaced relative to the grid along a coordinate axis.



Prescription for egg box effect

1. Filtering the sharp components of pseudopotential(PP)

•Fourier Filtering + Termination of PP

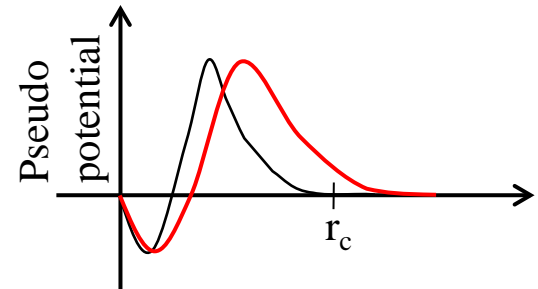
[R.D. King-Smith, M.C. Payne, & J.S. Lin PRB44 13063 (1991).]

Ignore the coefficients of large wave vectors using Fourier transform.

Vanish the pseudopotential at the cutoff radius.

Sometimes degrade transferability.

Tuning of the filtering parameter is important.



•Increase the cutoff radius

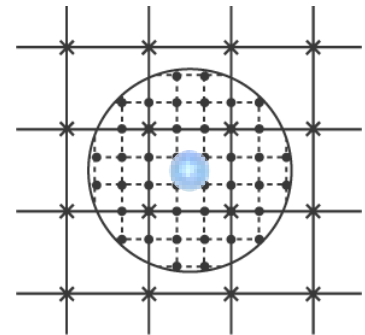
Obviously degrade transferability.

2. Implementing the integrations using denser grids

•Double-Grid Technique

[T. Ono & K. Hirose, PRL82 5016 (1999); PRB72 085115 (2005)]

Use denser grids in the vicinity of nuclei.

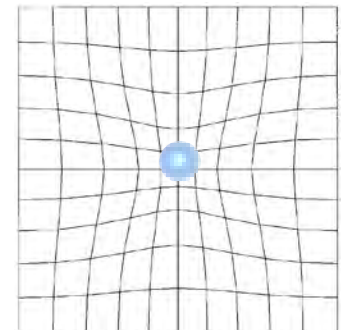


•Adaptive Coordinates

[F. Gygi & G. Galli, PRB52 R2229 (1995)]

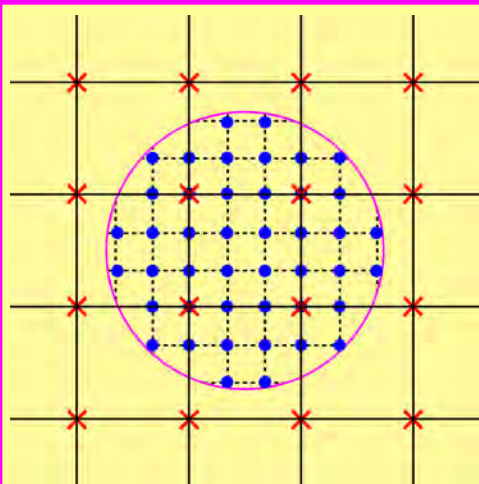
Use adaptive curvilinear coordinate.

Tuning of the coordinate parameters is indispensable.



Timesaving double grid method

T. Ono and K. Hirose, Phys. Rev. Lett. 82, 5016 (1999); Phys. Rev. B **72**, 085115 (2005).



x: coarse-grid points

•: dense-grid points

circle: cutoff region of pseudopotential of atom

Image of double grid

$$\int v_l(\mathbf{r})\psi(\mathbf{r})d\mathbf{r}$$

exactly defined on both coarse- and dense- grid points

defined only on coarse-grid points

Wave functions are interpolated as following

$$\psi(x_i) = \sum_I w_{I,i} \psi(X_I)$$

x_i : indexes of dense-grid points

X_I : indexes of coarse-grid points

Then

$$\int v_l(x)\psi(x)dx$$

$$= \sum_i v_l(x_i)\psi(x_i)h$$

$$= \sum_i v_l(x_i) \sum_I w_{I,i} \psi(X_I)h$$

$$= \sum_I \left\{ \sum_i w_{I,i} v_l(x_i)h \right\} \psi(X_I)$$

$W(X_I)$

"W" does not depend on wave functions but only on pseudopotentials.

The summation for numerical

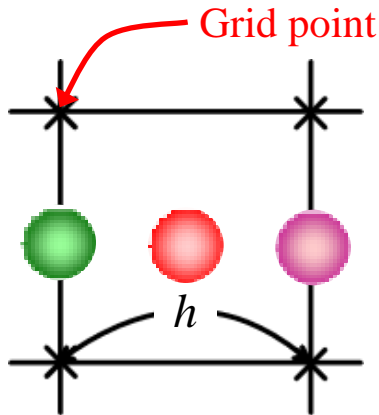
$$\sum_i \longrightarrow \sum_I$$

over dense grid

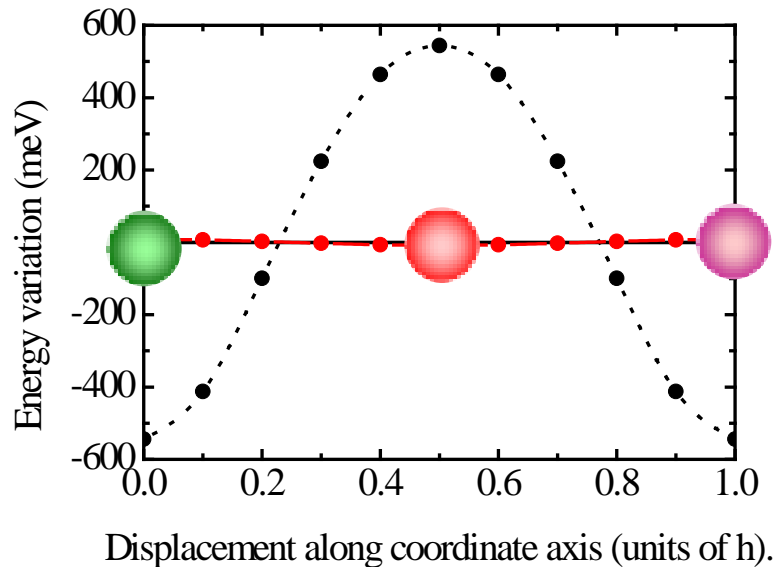
over coarse grid

Efficiency of the double grid

Example the case of oxygen atom



Oxygen atom is displaced relative to the grid along a coordinate axis.



Energy variation of CO_2

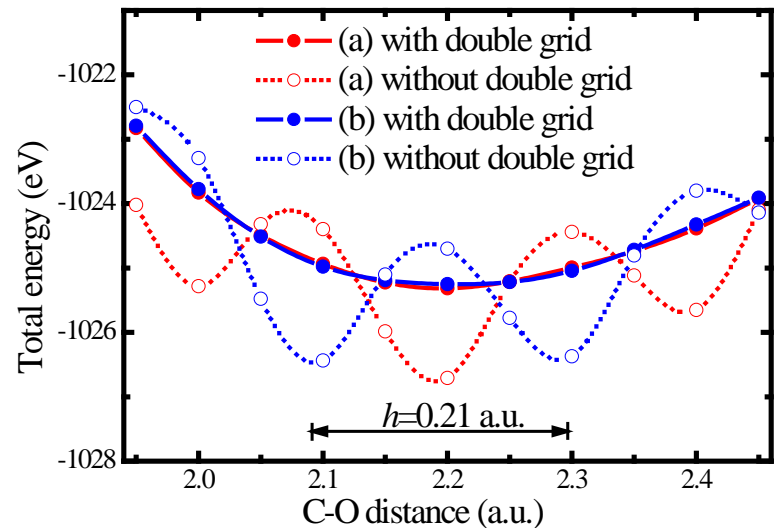
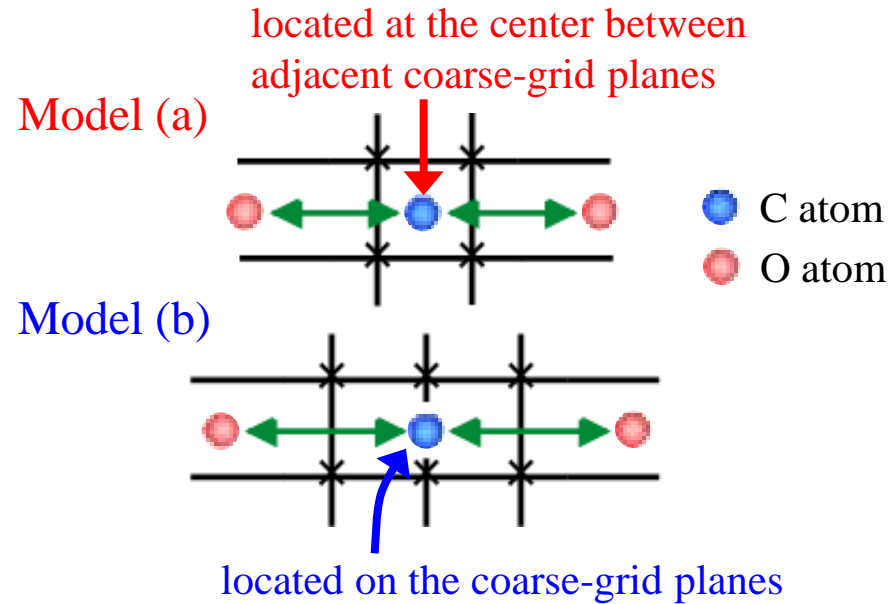


Table 5.1 Properties of diatomic molecules. The experimental data are from Huber and Herzberg (1979). The theoretical results are from our present calculation and from other methods using similar forms of the local-spin-density approximation.

	N ₂	O ₂	CO	F ₂
Bond length (a.u.)				
Experiment	2.07	2.28	2.13	2.68
This work	2.07	2.28	2.14	2.66
Other theory	2.07 [†]	2.27 [‡]	2.13 [†]	2.64 [†]
Vibrational mode (cm ⁻¹)				
Experiment	2358	1580	2169	892
This work	2400	1626	2160	1127
Other theory	2380 [‡]	1620 [‡]	2151 [†]	1051 [†]
Cohesive energy (eV)				
Experiment	9.76	5.12	11.09	1.60
This work	11.32	7.44	12.93	2.66
Other theory	11.6 [‡]	7.6 [‡]	12.8 [‡]	3.4 [‡]

[†]From Gygi and Galli (1995).

[‡]From Becke (1986, 1992).

Table 5.3 Calculated lattice constants, bulk moduli, and cohesive energies for bcc Na, fcc Al and diamond-structure Si.

	Na	Al	Si
Lattice constant (a.u.)			
Experiment	7.98 [†]	7.65 [†]	10.26 [†]
This work	7.70	7.63	10.19
Other theory	7.69 [‡]	7.58 [¶]	10.19 [§]
Bulk modulus (Mbar)			
Experiment	0.07 [†]	0.72 [†]	0.99 [†]
This work	0.09	0.74	0.96
Other theory	0.09 [‡]	0.72 [¶]	0.98 [§]
Cohesive energy (eV/atom)			
Experiment	1.11 [†]	3.39 [†]	4.63 [†]
This work	1.25	3.90	5.32
Other theory	1.21 [‡]	3.65 [¶]	5.9 [§]

[†]From Kittel (1986).

[‡]From Sigalas *et al.* (1990).

[¶]From Lam and Cohen (1981).

[§]From Holzwarth *et al.* (1997).

Table 5.4 Calculated lattice constants, bulk moduli, magnetic moments, and cohesive energies for ferromagnetic bcc Fe, fcc Co and Ni.

	Fe	Co	Ni
Lattice constant (a.u.)			
Experiment	5.42 [†]	6.69 [†]	6.65 [†]
This work	5.20	6.62	6.58
Other theory	5.22 [§]	6.52 [§]	6.48 [§]
Bulk modulus (Mbar)			
Experiment	1.68 [†]	1.87 [‡]	1.86 [†]
This work	2.68	2.50	2.70
Other theory	2.35 [§]	2.42 [§]	2.55 [§]
Magnetic moment (μ_B)			
Experiment	2.22 [†]	1.75 [¶]	0.61 [†]
This work	2.07	1.61	0.54
Other theory	2.05 [§]	1.52 [§]	0.59 [§]
Cohesive energy (eV/atom)			
Experiment	4.28 [†]	—	4.44 [†]
This work	6.06	6.47	6.86
Other theory	6.47 [§]	—	6.09 [§]

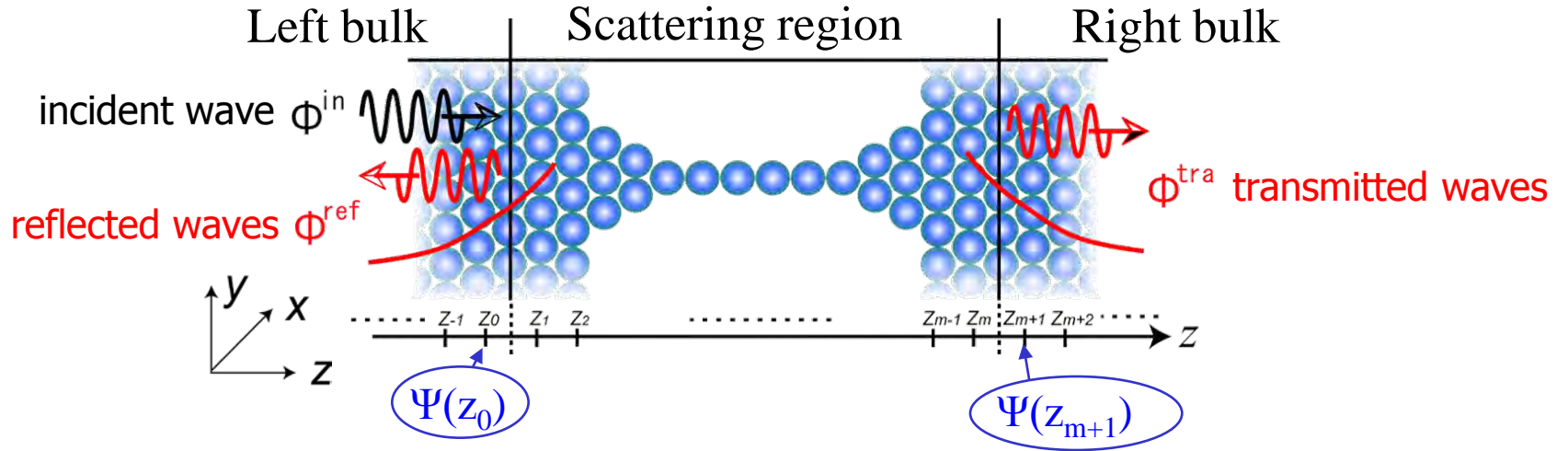
[†]From Kittel (1986).

[‡]From Guillermet and Grimvall (1989).

[¶]From Stearns (1986).

[§]From Moroni *et al.* (1997).

Overbridging boundary matching (OBM) method



Scattering boundary condition :

$$\Psi(z_k) = \begin{cases} \phi^{in}(z_k) + \sum_j C_j^{ref} \Phi_j^{ref}(z_k) & \dots \left(\begin{array}{l} \text{in the left electrode} \\ k \leq 0 \end{array} \right) \\ \sum_j C_j^{tra} \Phi_j^{tra}(z_k) & \dots \left(\begin{array}{l} \text{in the right electrode} \\ k \geq m+1 \end{array} \right) \end{cases}$$

Where $\Psi(z_k)$ and $\Phi(z_k)$ are M^2 columnar vectors defined by $\psi(r_{//}, z_k)$ and $\phi(r_{//}, z_k)$ on the plane $z=z_k$, respectively. (M^2 is the number of grid points on xy plane.)

$$\Psi(z_k) = [\psi(r_{11}, z_k), \dots, \psi(r_{M1}, z_k), \psi(r_{12}, z_k), \psi(r_{22}, z_k), \dots, \psi(r_{MM}, z_k)]^t,$$

$$\Phi^{ref(tra)}(z_k) = [\phi^{ref(tra)}(r_{11}, z_k), \dots, \phi^{ref(tra)}(r_{M1}, z_k), \phi^{ref(tra)}(r_{12}, z_k), \phi^{ref(tra)}(r_{22}, z_k), \dots, \phi^{ref(tra)}(r_{MM}, z_k)]^t.$$

Overbridging Boundary-Matching (OBM) method

The Kohn-Sham eq. in the area ($z=l \sim m$) covering over the **nanosturcture region** is written in a matrix form:

$$\left\{ \begin{array}{l} -B^\dagger \Psi_0 + (E - A_0) \Psi_1 - B \Psi_2 = 0 \\ -B^\dagger \Psi_1 + (E - A_1) \Psi_2 - B \Psi_3 = 0 \\ \vdots \\ -B^\dagger \Psi_{m-2} + (E - A_{m-1}) \Psi_{m-1} - B \Psi_m = 0 \\ -B^\dagger \Psi_{m-1} + (E - A_m) \Psi_m - B \Psi_{m+1} = 0 \end{array} \right\} \Rightarrow \underbrace{\begin{bmatrix} E - A_1 & -B & & & 0 \\ -B^\dagger & E - A_2 & -B & & \\ & \ddots & \ddots & \ddots & \\ & & \ddots & \ddots & -B^\dagger & E - A_{m-1} & -B \\ 0 & & & & -B^\dagger & E - A_m \end{bmatrix}}_{\equiv E - H} \begin{bmatrix} \Psi_1 \\ \Psi_2 \\ \vdots \\ \Psi_{m-1} \\ \Psi_m \end{bmatrix} = \begin{bmatrix} B^\dagger \Psi_0 \\ 0 \\ \vdots \\ 0 \\ B \Psi_{m+1} \end{bmatrix}$$

$\equiv E - H$ ↗ block tridiagonal matrix

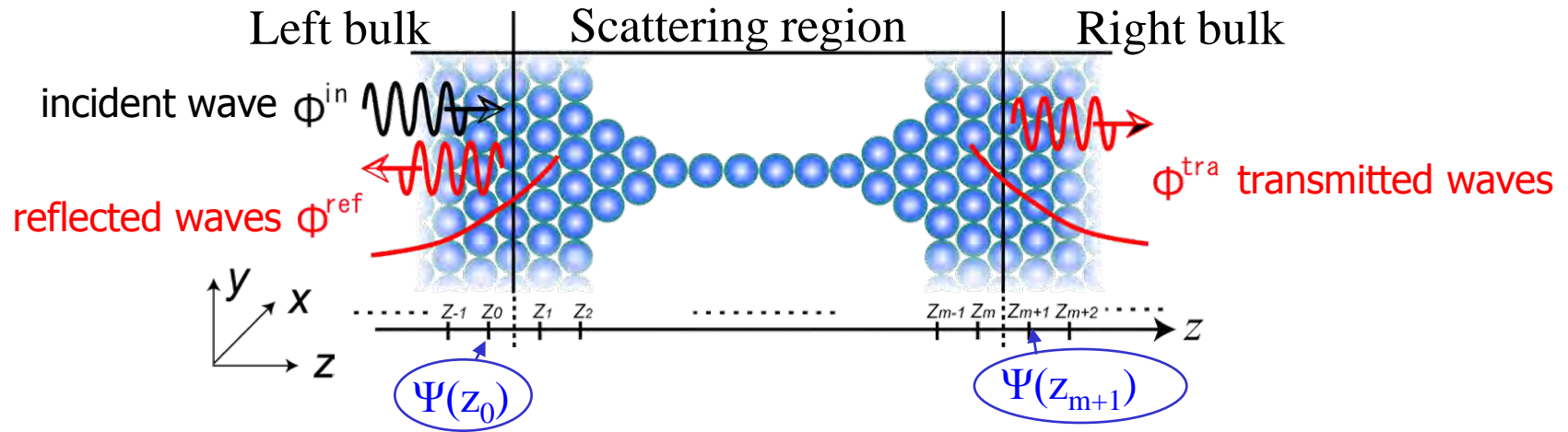
$$\begin{bmatrix} \Psi_1 \\ \Psi_2 \\ \vdots \\ \Psi_{m-1} \\ \Psi_m \end{bmatrix} = (E - H)^{-1} \begin{bmatrix} B^\dagger \Psi_0 \\ 0 \\ \vdots \\ 0 \\ B \Psi_{m+1} \end{bmatrix} \quad \text{where} \quad G = \begin{bmatrix} g_{1,1} & \cdots & g_{1,m} \\ g_{2,1} & & g_{2,m} \\ \vdots & & \vdots \\ g_{m-1,1} & & g_{m-1,m} \\ g_{m,1} & \cdots & g_{m,m} \end{bmatrix}$$

Then, Ψ_1 and Ψ_m are expressed in terms of Ψ_0 and Ψ_{m+1} as

$$\begin{pmatrix} \Psi_1 \\ \Psi_m \end{pmatrix} = \begin{pmatrix} g_{1,1} & g_{1,m} \\ g_{m,1} & g_{m,m} \end{pmatrix} \begin{pmatrix} B^\dagger \Psi_0 \\ B \Psi_{m+1} \end{pmatrix} \quad \dots\dots\dots (1)$$

G is Green function carrying all the information about the **nanosturcture region**.

Overbridging boundary matching (OBM) method



OBM formula to obtain transmission (reflection) coefficient C^{tra} (C^{ref}) :

$$\begin{pmatrix} g_{1,1}\Phi^{ref}(z_0) - \Phi^{ref}(z_1) & g_{1,m+1}\Phi^{tra}(z_{m+1}) \\ g_{m,1}\Phi^{ref}(z_0) & g_{m+1,m+1}\Phi^{tra}(z_{m+1}) - \Phi^{tra}(z_m) \end{pmatrix} \begin{pmatrix} C^{ref} \\ C^{tra} \end{pmatrix} = \begin{pmatrix} -g_{1,1}\phi^{in}(z_0) + \phi^{in}(z_1) \\ -g_{m,1}\phi^{in}(z_0) \end{pmatrix}$$

where g_{ij} is the block matrix of green function of the transition region determined by

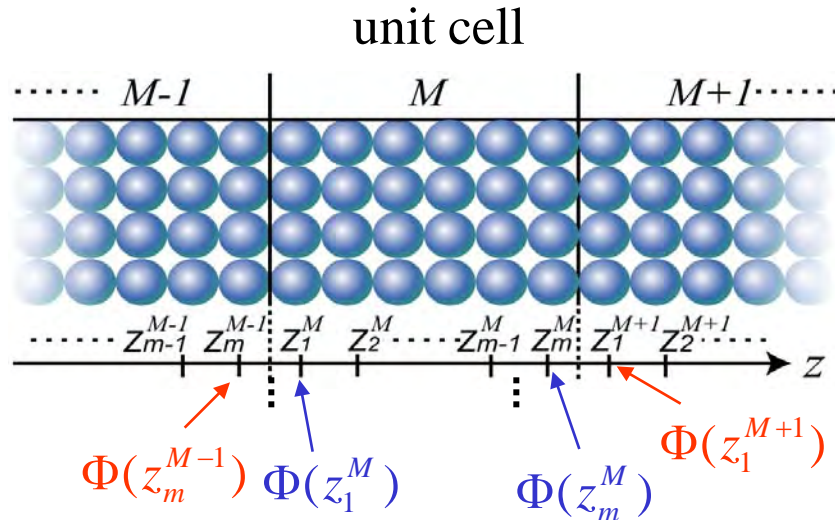
$$(E - H_{tran})^{-1} = \begin{bmatrix} g_{1,1} & g_{1,2} & \cdots & g_{1,m-1} & g_{1,m} \\ g_{2,1} & g_{2,2} & & g_{2,m-1} & g_{2,m} \\ \vdots & \vdots & \ddots & \vdots & \vdots \\ g_{m-1,1} & g_{m-1,2} & & g_{m-1,m-1} & g_{m-1,m} \\ g_{m,1} & g_{m,2} & \cdots & g_{m,m-1} & g_{m,m} \end{bmatrix}.$$

$E - H_{tran}$ is also sparse matrix in the RSFD, the algorithm to compute the Green functions is easy to be parallelized using conjugate gradient method.

Calculation method of the bulk wave functions

(generalized Bloch functions) Φ in the bulk

We next derive the formula to determine the wave functions in the bulk region where the potential is periodic along the z direction.



Along the same line mentioned above, we obtain the relation

$$\begin{pmatrix} \Phi(z_1^M) \\ \Phi(z_m^M) \end{pmatrix} = \begin{pmatrix} g_{1,1} & g_{1,m} \\ g_{m,1} & g_{m,m} \end{pmatrix} \begin{pmatrix} B^\dagger \Phi(z_m^{M-1}) \\ B \Phi(z_1^{M+1}) \end{pmatrix} \quad (1)$$

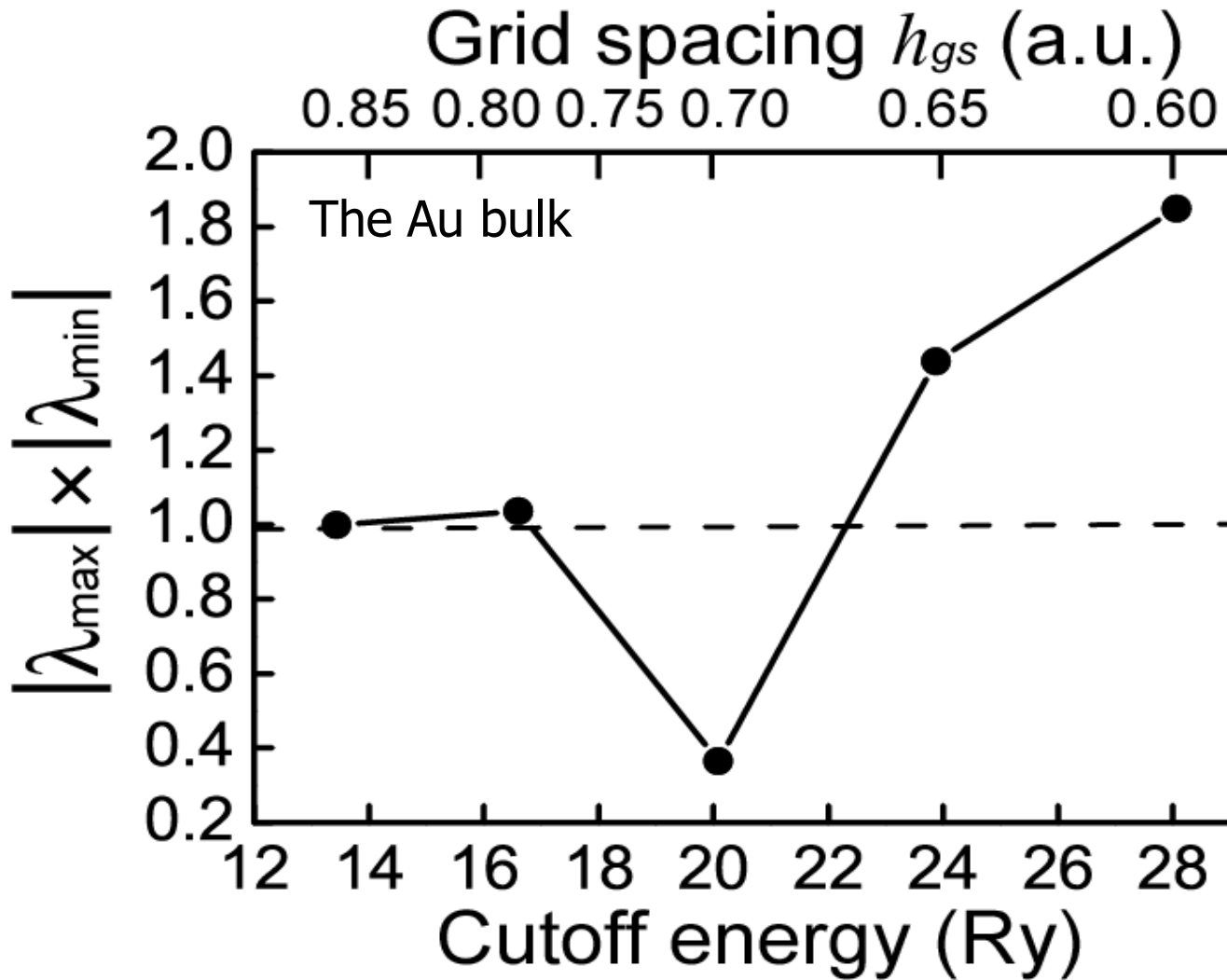
The other restriction is the generalized Bloch condition due to the periodicity along the z direction: $\Phi(z_1^{M+1}) = \lambda \Phi(z_1^M)$ and $\Phi(z_m^M) = \lambda \Phi(z_m^{M-1})$ (2)

Here $\lambda = e^{ik_z L}$, where k_z is complex number and L is the z length of the unit cell.

From Eqs. (1) and (2), we obtain generalized eigenvalue equation

$$\Pi_1 \begin{pmatrix} \Phi(z_m^{M-1}) \\ \Phi(z_1^{M+1}) \end{pmatrix} = \lambda \Pi_2 \begin{pmatrix} \Phi(z_m^{M-1}) \\ \Phi(z_1^{M+1}) \end{pmatrix}, \text{ where } \Pi_1 = \begin{pmatrix} g_{m,1} B^+ & g_{m,m} B \\ 0 & I \end{pmatrix}, \quad \Pi_2 = \begin{pmatrix} I & 0 \\ g_{1,1} B^+ & g_{1,m} B \end{pmatrix}$$

Numerical limitation of the generalized eigenvalue equation



The higher cutoff energy is taken, the more numerical errors accumulate!

The way to overcome the numerical difficulty caused by evanescents

Left-bulk region

b.c. in left-bulk region (for $k \leq 0$) :

$$\Psi(z_k) = \phi^{in}(z_k) + \sum_l r_l \Phi_l^{ref}(z_k). \quad (3)$$

In terms of the matrix
made of reflection wave functions

$$\hat{\Phi}^{ref}(z) = [\Phi_1^{ref}(z), \Phi_2^{ref}(z), \dots, \Phi_N^{ref}(z)], \quad (5)$$

we define the ratio matrix as

$$R^{ref}(z_0) = \hat{\Phi}^{ref}(z_{-1}) \hat{\Phi}^{ref}(z_0)^{-1}. \quad (6)$$

From Eqs.(3) and (6)

$$\Psi(z_0) - \phi^{in}(z_0) = R^{ref}(z_0)^{-1} [\Psi(z_{-1}) - \Phi^{in}(z_{-1})]. \quad (7)$$

Right-bulk region

b.c. in right-bulk region (for $k \geq m+1$) :

$$\Psi(z_k) = \sum_l t_l \Phi_l^{tra}(z_k). \quad (4)$$

In terms of the matrix
made of transmission wave functions

$$\hat{\Phi}^{tra}(z) = [\Phi_1^{tra}(z), \Phi_2^{tra}(z), \dots, \Phi_N^{tra}(z)], \quad (8)$$

we define the ratio matrix as

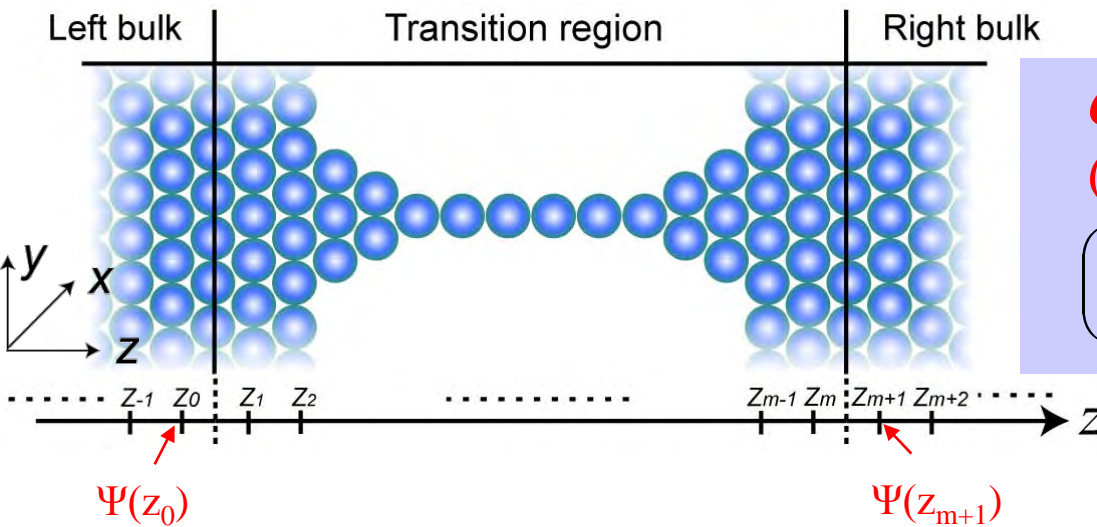
$$R^{tra}(z_{m+2}) = \hat{\Phi}^{tra}(z_{m+2}) \hat{\Phi}^{tra}(z_{m+1})^{-1}. \quad (9)$$

From Eqs.(4) and (9)

$$\Psi(z_{m+1}) = R^{tra}(z_{m+2})^{-1} \Psi(z_{m+2}). \quad (10)$$

The ratio matrices, which correspond to logarithmic derivatives mathematically, include the ratios of *evanescent* waves at two adjacent z_k points, being **free from numerical errors** caused by *evanescent* waves.

The way to overcome the numerical difficulty caused by evanescents



Overbridging boundary-matching (OBM) formula

$$\begin{pmatrix} \Psi(z_1) \\ \Psi(z_m) \end{pmatrix} = \begin{pmatrix} g_{1,1} & g_{1,m} \\ g_{m,1} & g_{m,m} \end{pmatrix} \begin{pmatrix} B^\dagger \Psi(z_0) \\ B \Psi(z_{m+1}) \end{pmatrix} \quad (1)$$

$$\begin{bmatrix} \Psi(z_1) - \phi^{in}(z_1) \\ \Psi(z_0) - \phi^{in}(z_0) \end{bmatrix} = R^{ref}(z_1)^{-1} \begin{bmatrix} \Psi(z_0) - \phi^{in}(z_0) \\ \Psi(z_{m+1}) - \phi^{in}(z_{m+1}) \end{bmatrix} \quad (7)$$

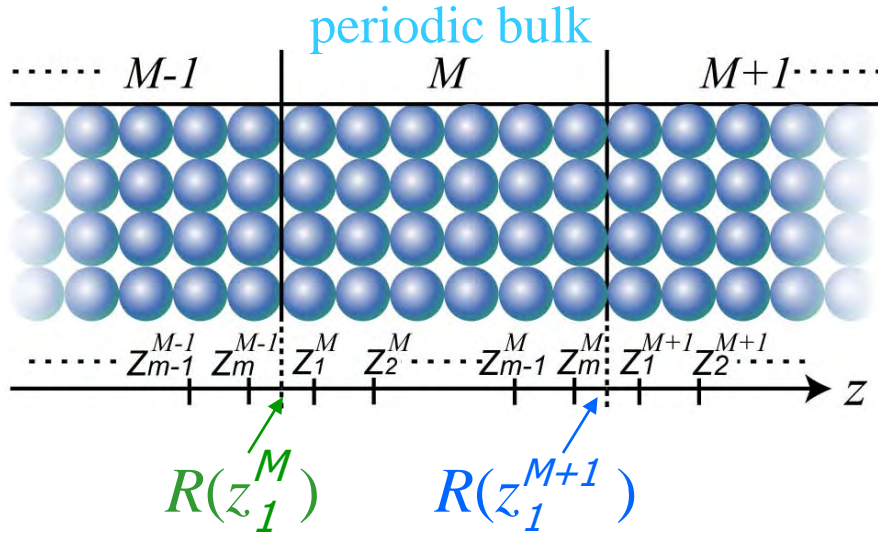
$$\Psi(z_m) = R^{tra}(z_{m+1})^{-1} \Psi(z_{m+1}) \quad (10)$$

Inserting Eqs. (7) and (10) into Eq. (1), we obtain **the final form of our overbridging boundary-matching (OBM) formula** in terms of the ratio matrices R 's

$$\begin{pmatrix} g_{1,1}^\dagger B - R^{ref}(z_1)^{-1} & g_{1,m} B \\ g_{m,1}^\dagger B & g_{m,m} B - R^{tra}(z_{m+1})^{-1} \end{pmatrix} \begin{pmatrix} \Psi(z_0) \\ \Psi(z_{m+1}) \end{pmatrix} = \begin{pmatrix} -R^{ref}(z_1)^{-1} \phi^{in}(z_0) + \phi^{in}(z_1) \\ 0 \end{pmatrix} \quad (11)$$

output input values incident propagating Bloch wave

The way to directly compute the ratio matrix R ,
not via the calculation of evanescent waves themselves



**Overbridging boundary-matching
(OBM) formula**

$$\begin{pmatrix} \Phi(z_1^M) \\ \Phi(z_m^M) \end{pmatrix} = \begin{pmatrix} g_{1,1} & g_{1,m} \\ g_{m,1} & g_{m,m} \end{pmatrix} \begin{pmatrix} B^\dagger \Phi(z_m^{M-1}) \\ B \Phi(z_1^{M+1}) \end{pmatrix} \quad (1)$$

From Eq. (1), we obtain

$$\begin{cases} \Phi(z_1^M) \Phi^{-1}(z_m^{M-1}) = g_{1,1}^M B^+ + g_{1,m}^M B \Phi(z_1^{M+1}) \Phi^{-1}(z_m^{M-1}) \end{cases} \quad (12)$$

$$\begin{cases} \Phi(z_m^M) \Phi^{-1}(z_1^{M+1}) = g_{m,1}^M B^+ \Phi(z_m^{M-1}) \Phi^{-1}(z_1^{M+1}) + g_{m,m}^M B \end{cases} \quad (13)$$

Inserting Eq. (13) into Eq. (12),

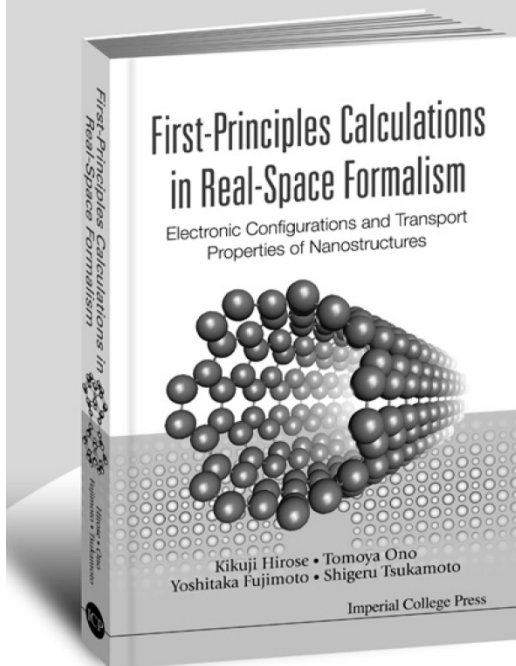
$$R(z_1^{M+1}) = g_{m,m}^M B + g_{m,1}^M B^+ \left[R(z_1^M)^{-1} - g_{1,1}^M B^+ \right]^{-1} g_{1,m}^M B \quad (14)$$

The Bloch condition $\hat{\Phi}(z_1^{M+1}) = \lambda \hat{\Phi}(z_1^M)$ reads as $R(z_1^{M+1}) = R(z_1^M)$. (15)

The solution R of the **continued-fraction** eq. under the constraint $R(z_1^{M+1}) = R(z_1^M)$ can always be determined in a self-consistent manner.

First-Principles Calculations in Real-Space Formalism

Electronic Configurations and Transport Properties of Nanostructures



by

Kikuji Hirose

(Osaka University, Japan)

Tomoya Ono

(Osaka University, Japan)

Yoshitaka Fujimoto

(University of Tokyo, Japan)

Shigeru Tsukamoto

(National Institute for Materials Science, Japan)

With cutting-edge materials and minute electronic devices being produced by the latest nanoscale fabrication technology, it is essential for scientists and engineers to rely on first-principles (ab initio) calculation methods to fully understand the electronic configurations and transport properties of nanostructures. It is now imperative to introduce practical and tractable calculation methods that accurately describe the physics in nanostructures suspended between electrodes.

This timely volume addresses novel methods for calculating electronic transport properties using real-space formalisms free from geometrical restrictions. The book comprises two parts: The first details the basic formalism of the real-space finite-difference method and its applications. This provides the theoretical foundation for the second part of the book, which presents the methods for calculating the properties of electronic transport through nanostructures sandwiched by semi-infinite electrodes.

Contents: Real-Space Finite-Difference Method for First-Principles Calculations: Foundations of Methodology; Solvers of the Poisson Equation and Related Techniques; Minimization Procedures of the Energy Functional; Timesaving Double-Grid Technique; Implementation for Systems under Various Boundary Conditions; **Electronic Transport Through Nanostructures Between Semi-Infinite Electrodes:** Basic Scheme of the Overbridging Boundary-Matching Method; Inclusion of Norm-Conserving Pseudopotentials; Jellium Electrode Approximation; Green's Function Formalism and the Overbridging Boundary-Matching Scheme; Calculation Method Based on the Lippmann-Schwinger Equation; **Appendices:** Formulas for Long-Range Potentials under Various Boundary Conditions; Tight-Binding Approach Based on the Overbridging Boundary-Matching Scheme.

Key Features

- Presents details of methods, as well as some applications, using accurate schemes for examining electronic configurations and conduction properties
- Information and insight about nanoscale electronic transport using a newly developed method based on first-principles

Readership: Graduate and post-graduate students and researchers in computational, quantum and condensed matter physics, and nanoscience.

264pp
1-86094-512-0

Jan 2005
US\$68 £41

 **World Scientific**
www.worldscientific.com

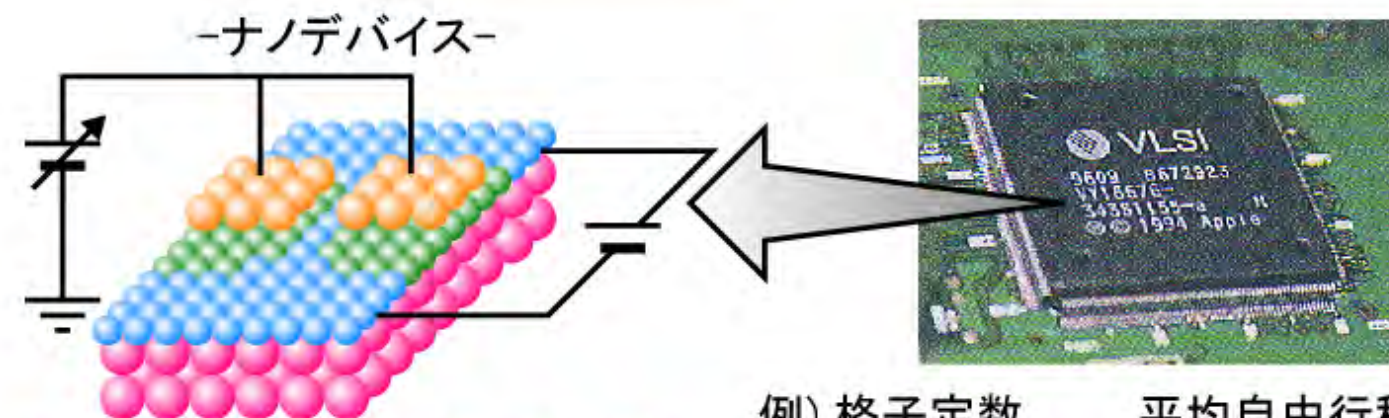
 **Imperial College Press**
www.icpress.co.uk

本書はネット販売のAmazonでも購入できます。

研究の背景

電子デバイスのダウンサイジング

単電子トランジスタのような単電子制御の量子デバイスの実現

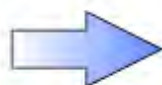


ナノ構造 \ll 電子の平均自由行程

例)	格子定数	平均自由行程
Si	5.428 \AA	\ll 約 400 \AA (室温)
Au	4.078 \AA	\ll 約 500 \AA (室温)

格子振動や結晶欠陥による電子の散乱やエネルギーの散逸がほとんどなくなる領域

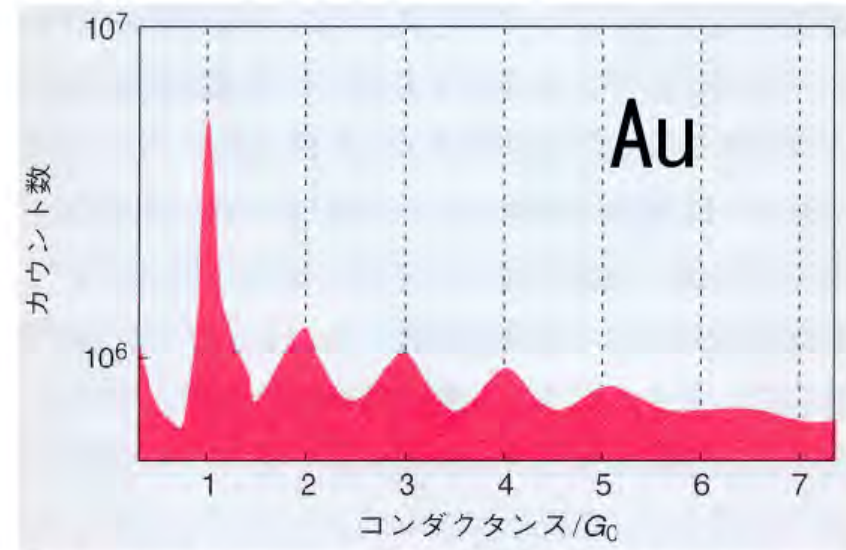
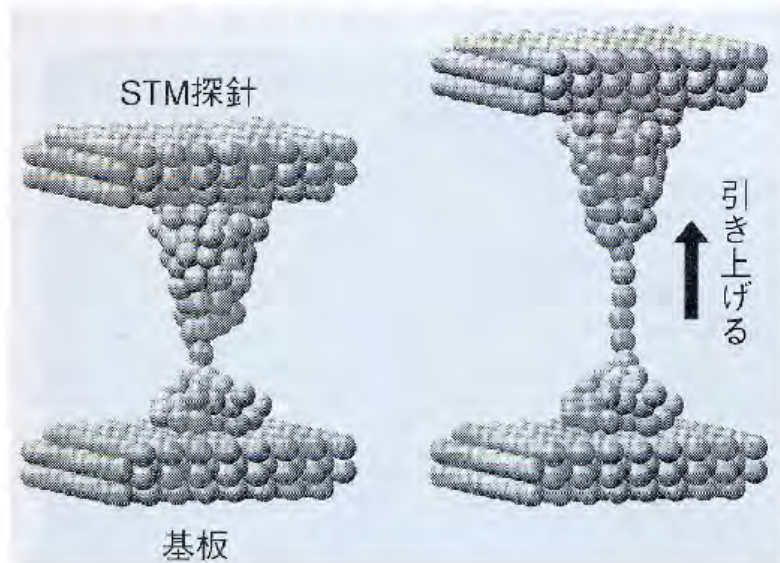
電子の運動 \Rightarrow 弾道(Ballistic)伝導
電子の量子的性質があらわになる



特異な電子輸送特性が観測される

これを実験的・理論的に解析する必要がある

走査型トンネル顕微鏡 (STM)



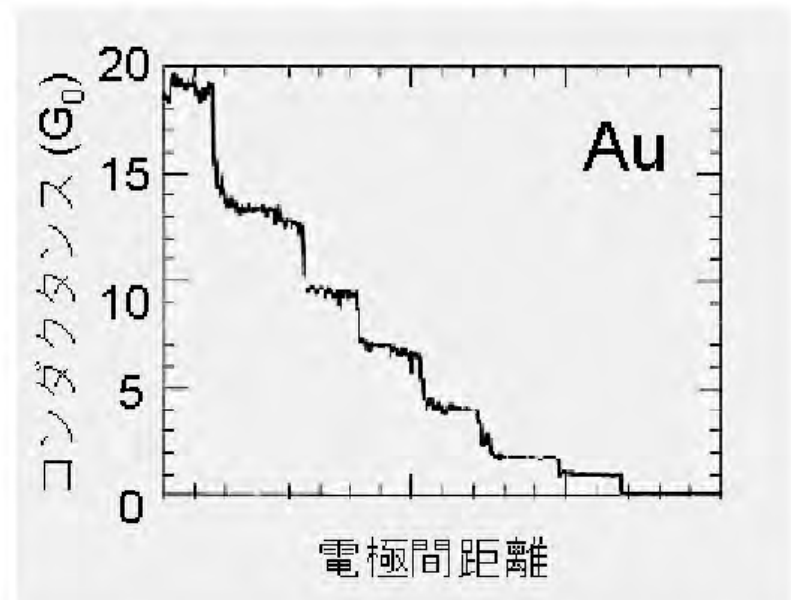
J.L.Costa-Kramer *et al.*, PRB **55**, 12910 (1997)

コンダクタンスの量子化単位

$$G_0 = 2e^2/h$$

(e : 電荷素量, h : プランク定数)

機械的に形成した金属微小接合における
コンダクタンスの量子化の実験例

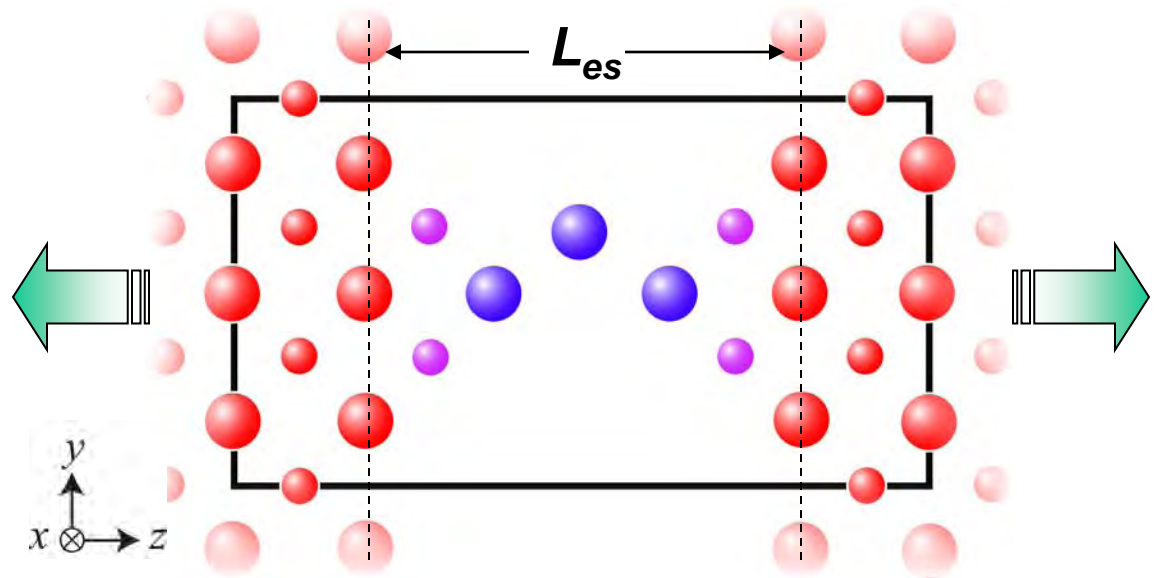


Rubio *et al.*, PRL **76** 2302 (1996)

Example 1: Conduction properties of sodium nanowires

Computational Model

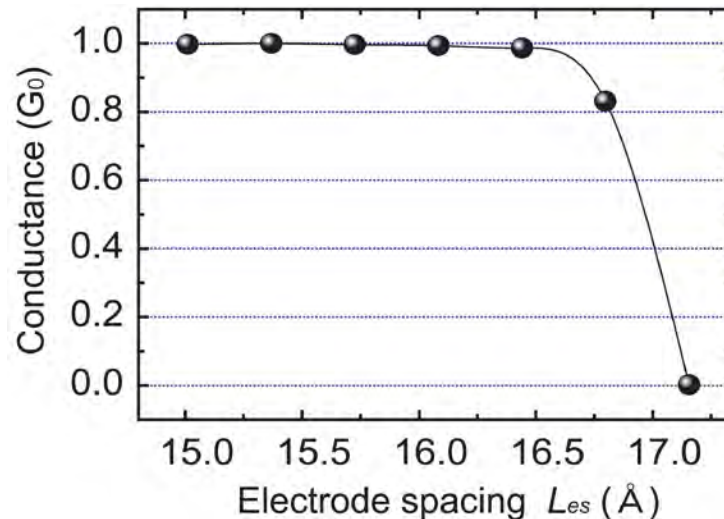
- 電極原子
- 台座原子
- 単原子鎖原子



Variation of the conductance w.r.t. electrode spacing L_{es}

Quantized unit of conductance

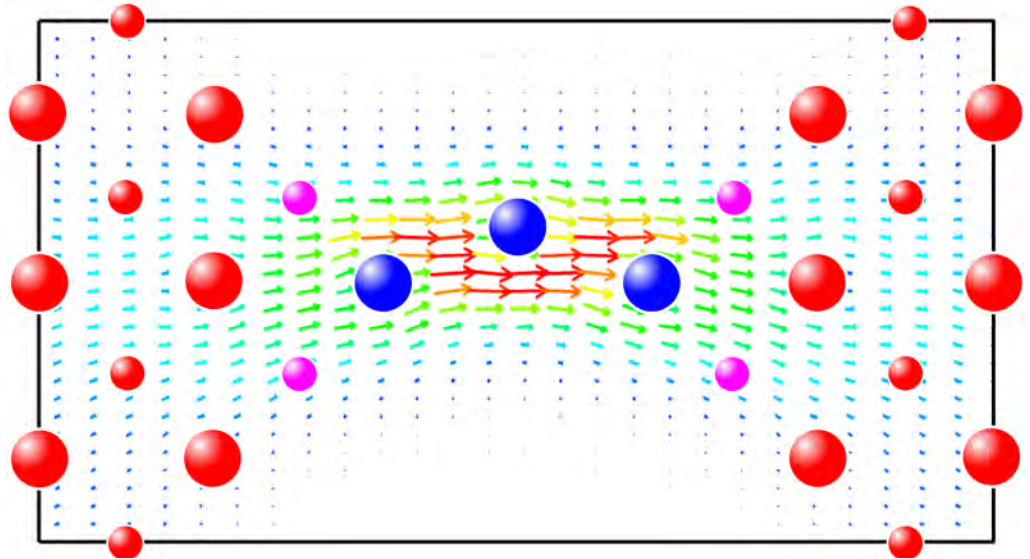
$$G_0 = \frac{2e^2}{h}$$



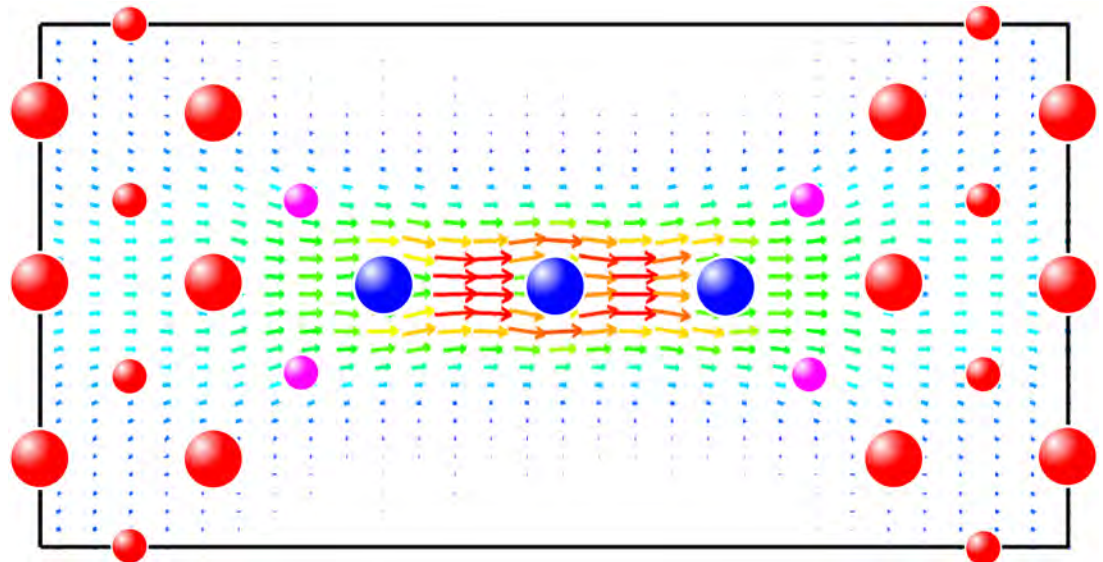
Y. Egami, T. Sasaki, T. Ono, and K. Hirose, Nanotechnology, **16**, S161 (2005).

Current density distribution

$L_{es}=15.0$



$L_{es}=16.4$

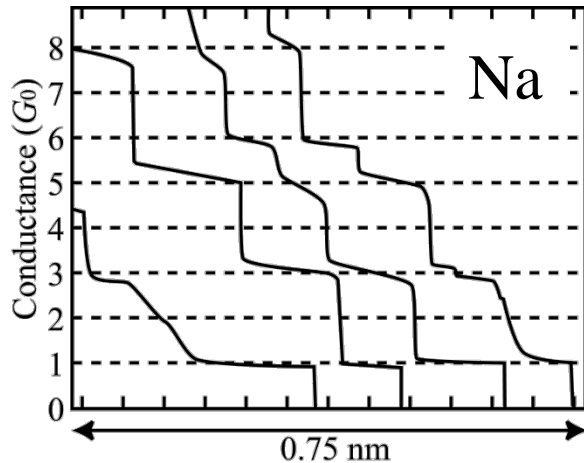


[010]
↑
[001]
→

LOW HIGH

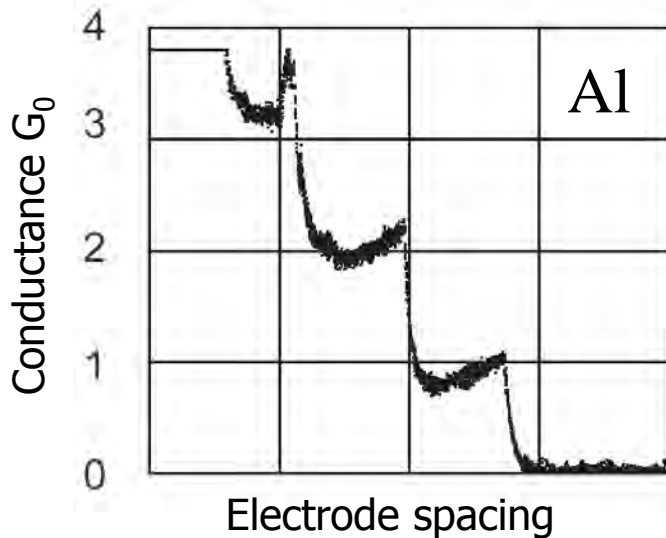
Example 2: Al nanowire under elongation

Experimental background



L. M. Krans *et al.*,
Nature **375**, 767 (1995)

For the nanowire made of **monovalent** atoms, the trace of the electronic conductance exhibits **plateaus**.

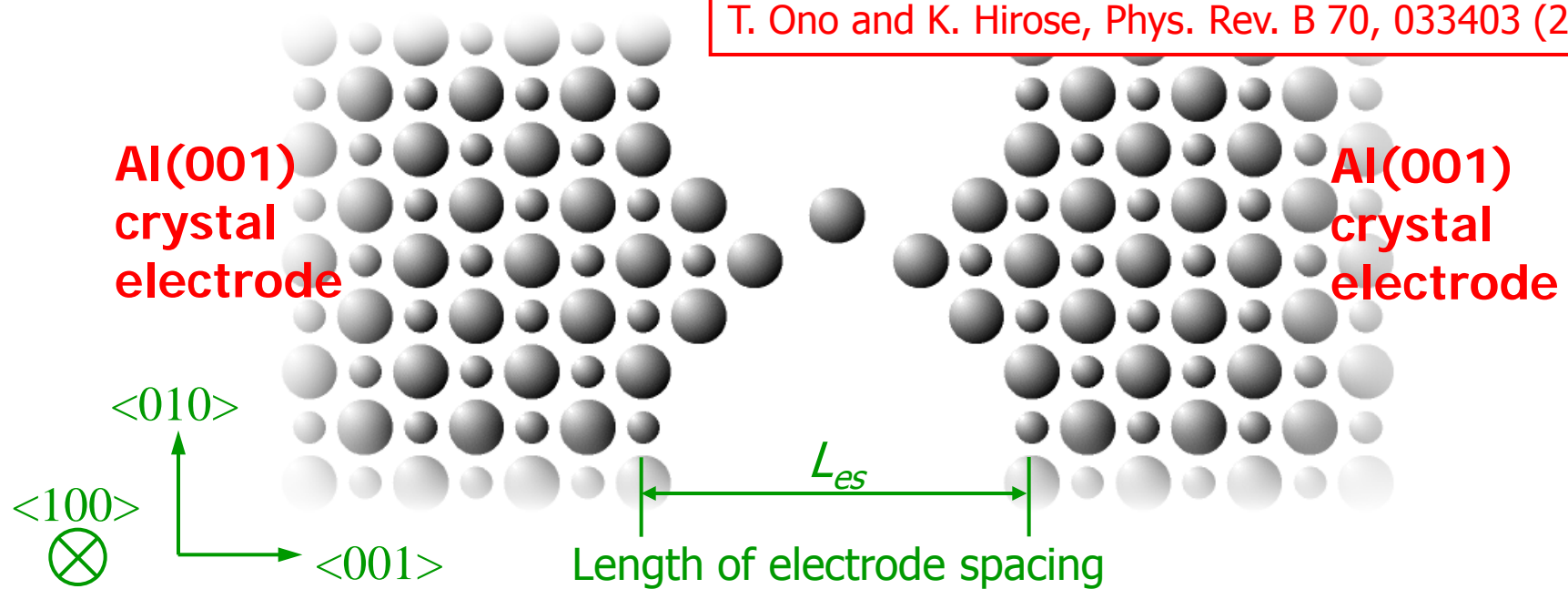


For the nanowire made of **multivalent** atoms, the trace of the electronic conductance exhibits **convex downward curves**.

J. Mizobata, A. Fujii, S. Kurokawa and A. Sakai,
J. Jpn. Appl. Phys. 42, 4680 (2003)

3-atom aluminum nanowire

T. Ono and K. Hirose, Phys. Rev. B 70, 033403 (2004).

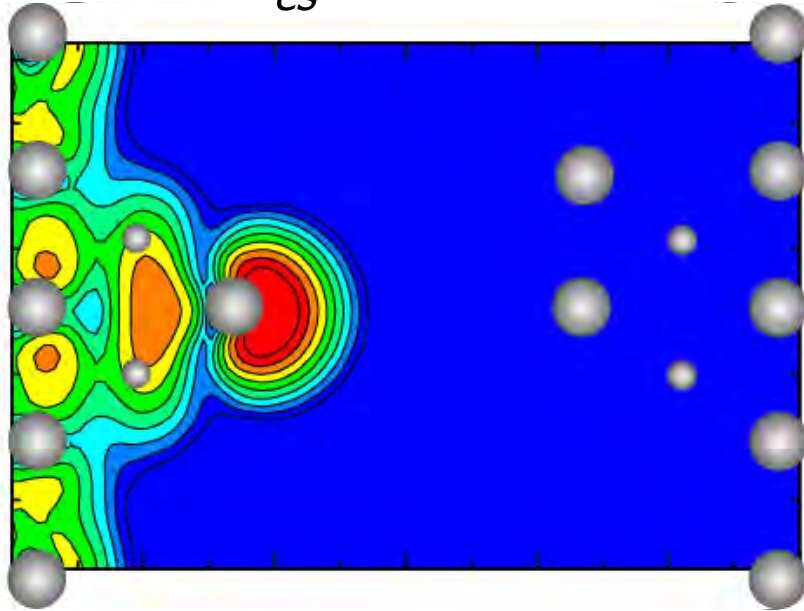


Computational conditions

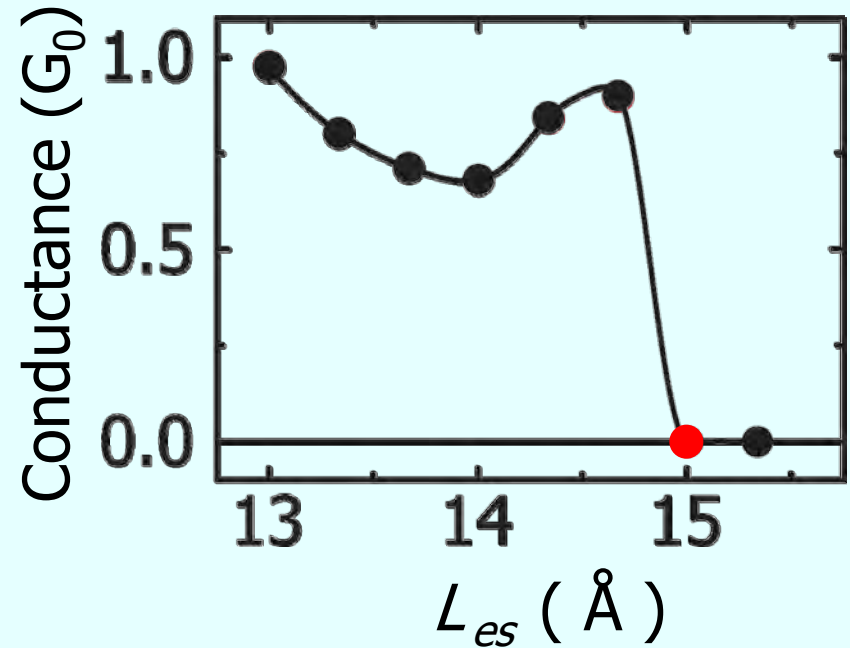
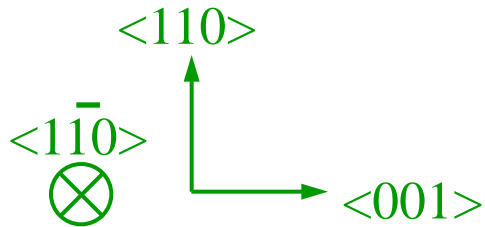
- Grid spacing 0.33 Å (Cutoff energy 25 Ry)
- Periodic boundary conditions are imposed at x and y directions. (The cell size is $L_x=8.0$ Å and $L_y=8.0$ Å.)
- Electrode spacing (average interatomic distance)
 $13.00\text{Å} < L_{es} < 15.34\text{Å}$ ($2.50\text{Å} < d_{av} < 3.67\text{Å}$).
($d_{av}=2.75$ Å is the nearest neighbor atomic distance in Al crystal.)
- Only atom locates at the center of the nanowire
is optimized on (110) plane by molecular-dynamics simulation
- Norm conserving pseudopotential (NCPS97) is adopted.

Conductance of Al nanowire

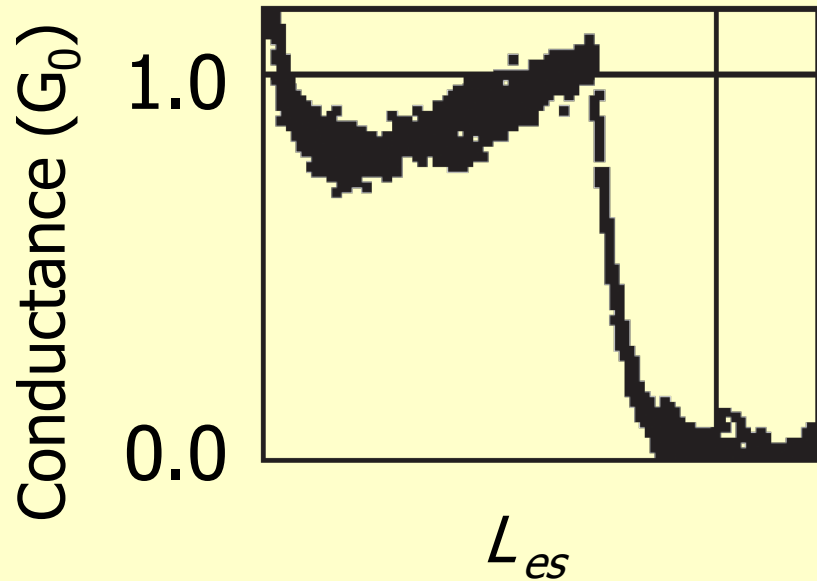
$$L_{es} = 15.00 \text{ \AA}$$



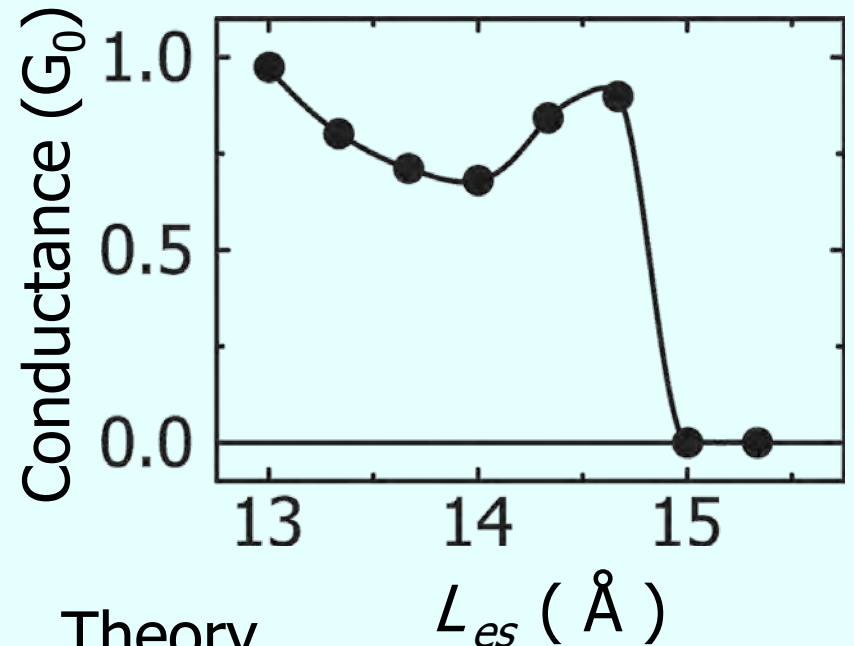
Current-electron distribution



Conductance of Al nanowire



Experiment

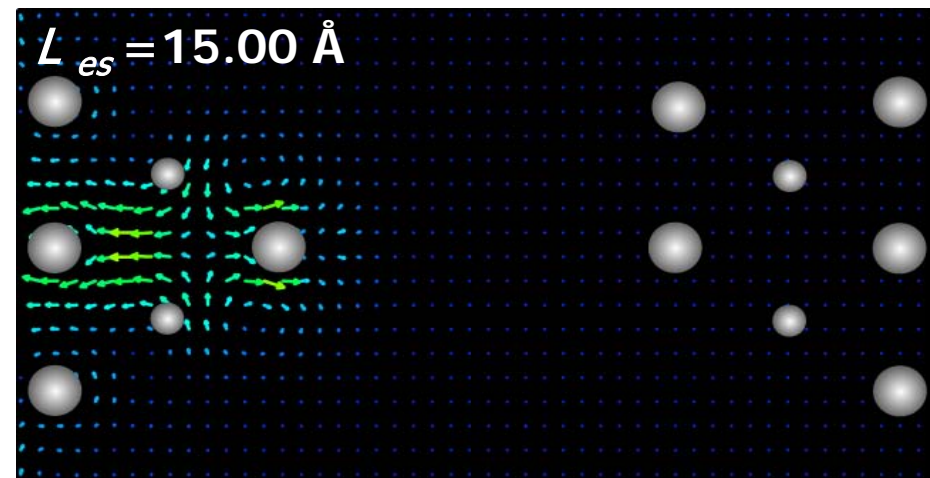
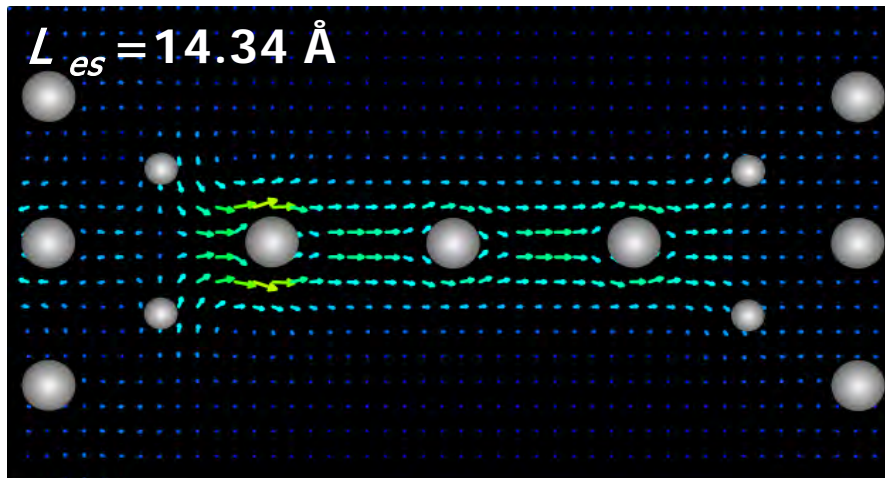
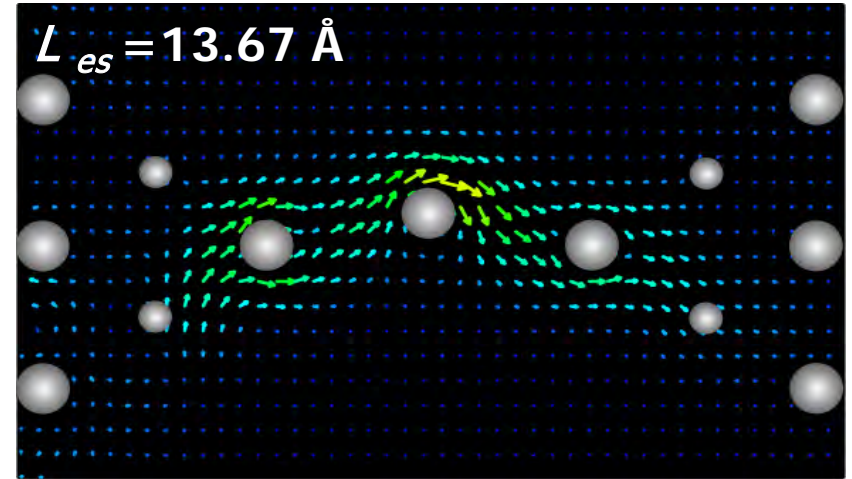
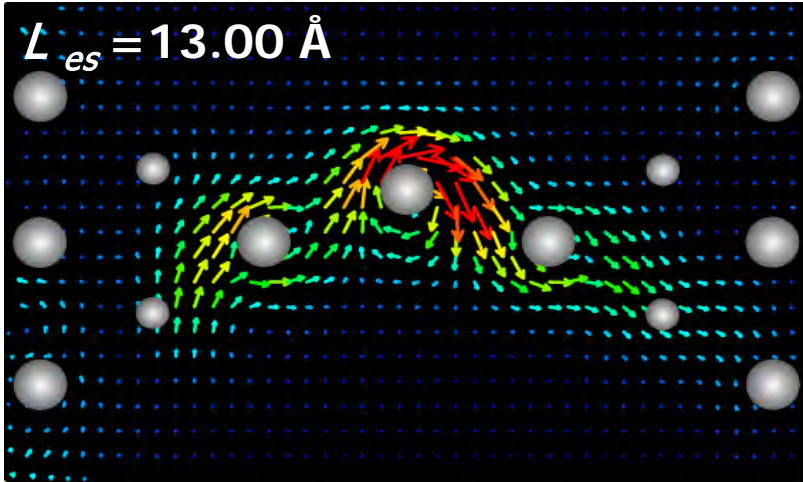


Theory

J. Mizobata, A. Fujii, S. Kurokawa and A. Sakai,
J. Jpn. Appl. Phys. 42, 4680 (2003)

- The conductance before breaking is approximately $1 G_0$ in both experimental and theoretical studies.
- The plateau is not flat but show a convex downward curve.

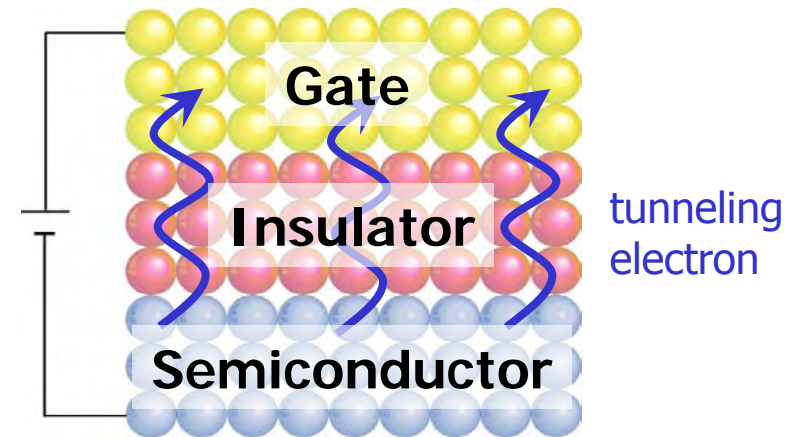
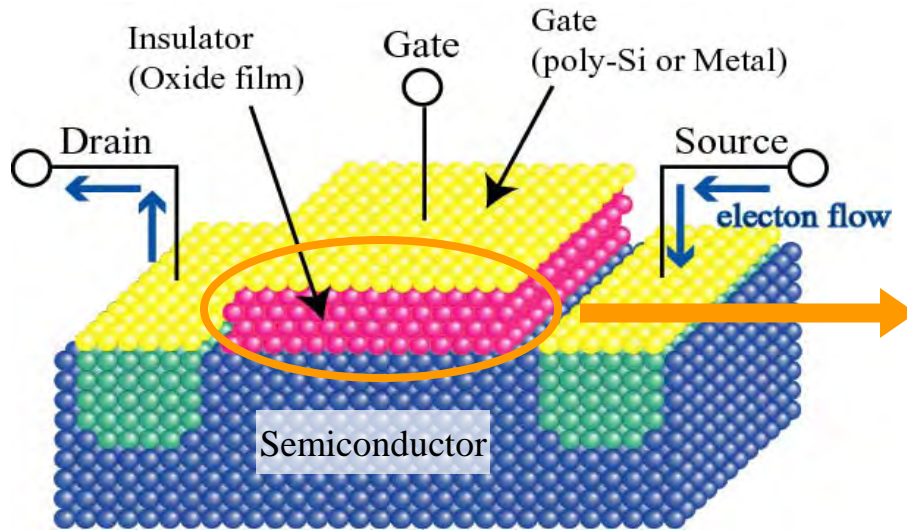
Electric current flows



- Incident electrons predominantly enter the bent wire along the atom rows in the $[0\bar{1}1]$ and $[101]$ directions, flow through the p_x and p_y orbitals of the center atom, and consequently form loop current rotating around the center atom.

Example 3: Leakage current through silicon oxide films

T. Ono, Phys. Rev. B 79 195326 (2009).



Metal Oxide Semiconductor Field Effect Transistor (MOSFET)

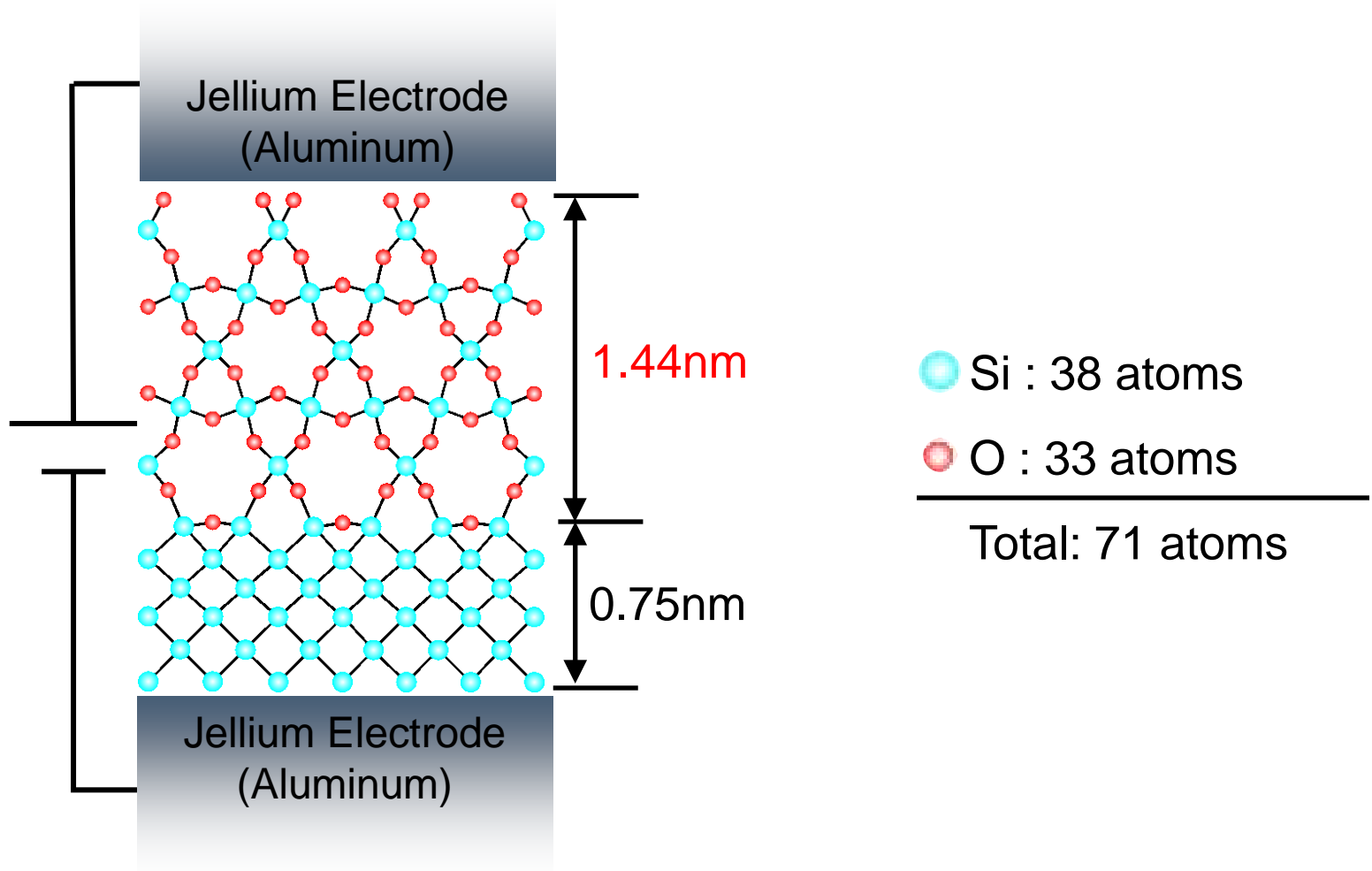
VLSI (very large scale integration) technology is in need of an atomic scale understanding of issues arising from the miniaturization of silicon devices.

The understanding and control of leakage current of the Si/SiO₂ interface are key subjects.

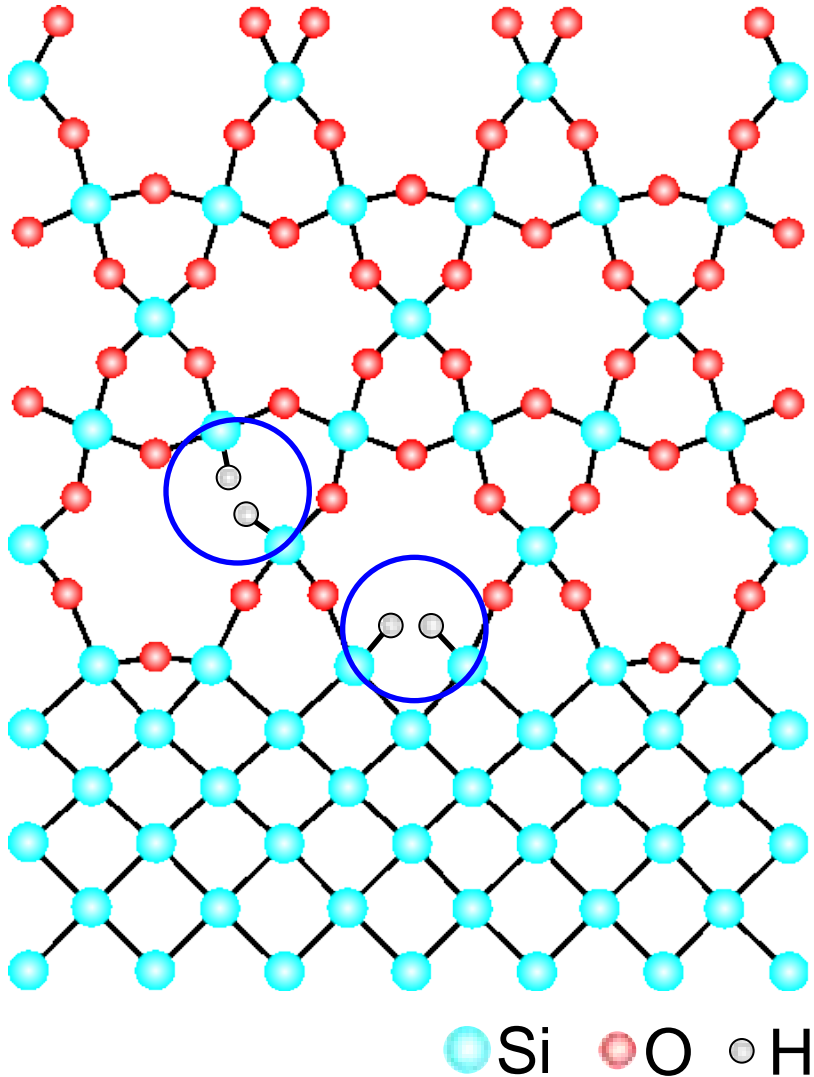
Computational Model

3ML α -quartz(001) Si/SiO₂ interface.

H. Kageshima & K. Shiraishi, PRL, **81**, 5936(1998).



Hydrogen Atoms in Si/SiO₂



The silicon oxidation process with annealing in oxygen ambient makes lots of O vacancies in the film. ($\sim 10^{12}/\text{cm}^2$)



Annealing of the SiO₂ films in hydrogen ambient reduces the defects in SiO₂ films and at the interface. ($10^9 \sim 10^{10}/\text{cm}^2$)



The terminating H atoms are released by hot electron in real devices.



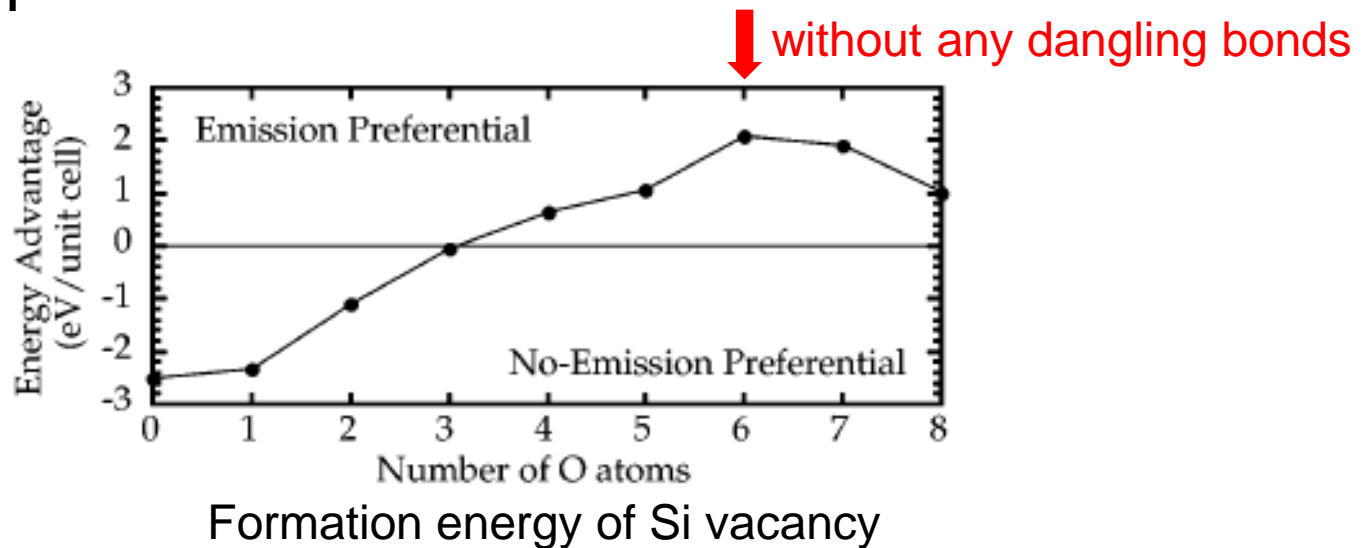
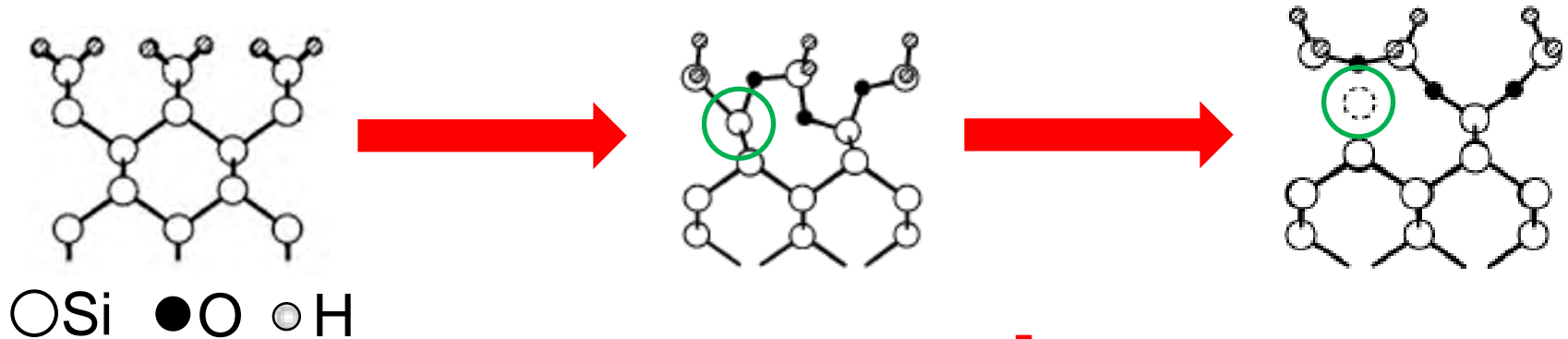
The dangling bonds degrade the dielectric reliability and the device performance.

Oxidation process of silicon surface

H. Kageshima & K. Shiraishi, PRL, **81**, 5936(1998).

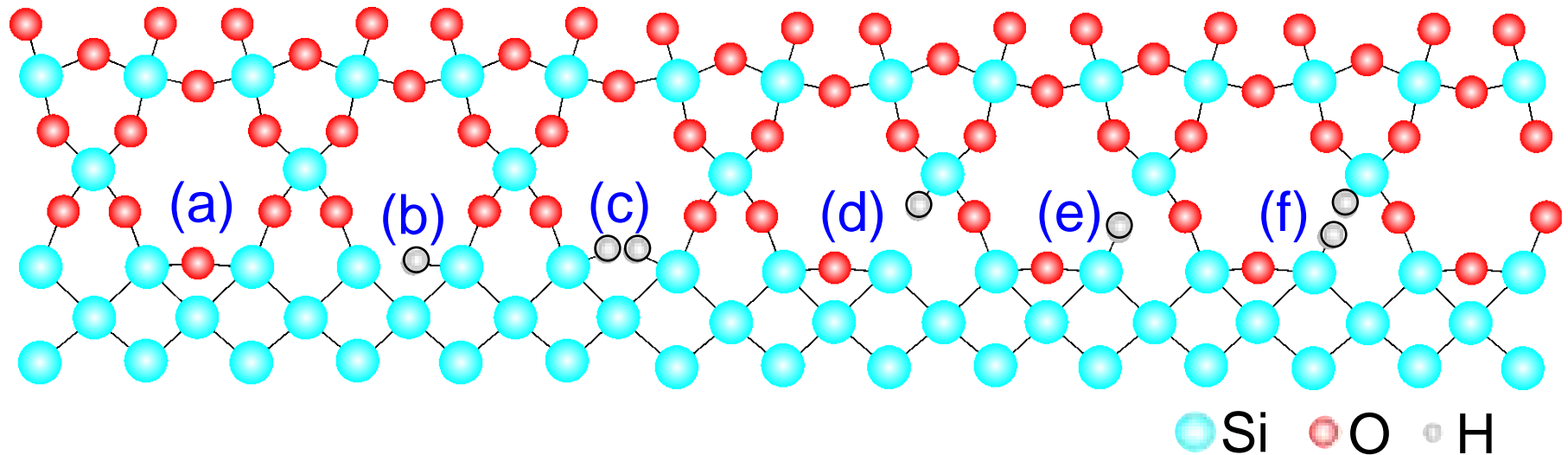
Insert oxygen atom
between Si-Si bonds

Stress is released by
emission of silicon atoms.



Si atoms are emitted even when the number of inserted O atoms is 5.
But, vacancies become interface defects.

Defects Included at Interfaces

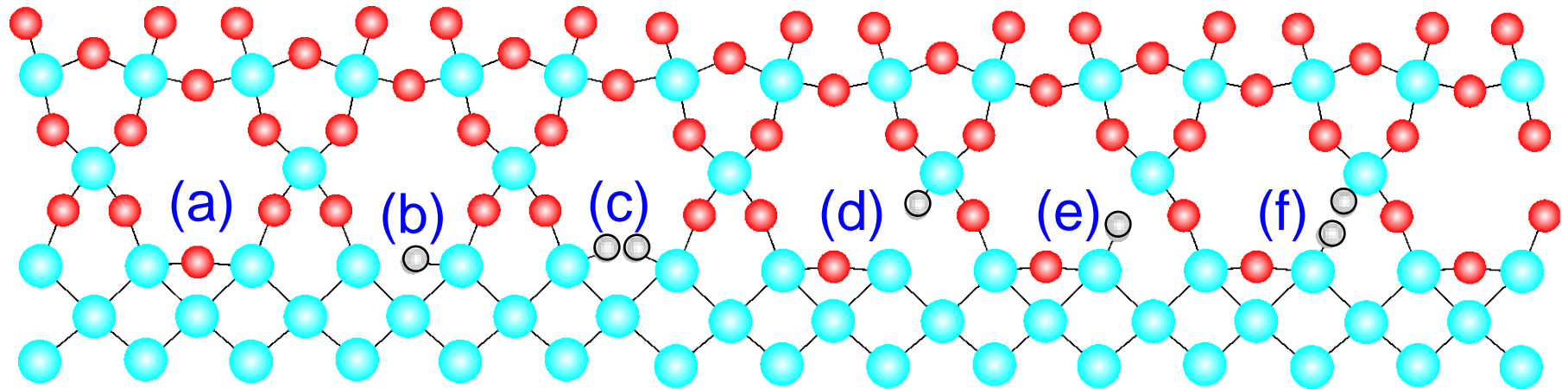


- (a) Without defects
- (b) O at the interface is replaced by H
- (c) Dangling bond in (b) is terminated by H
- (d) O at the second layer of the interface is replaced by H
(H terminates the dangling bond of upper Si)
- (e) O at the second layer of the interface is replaced by H
(H terminates the dangling bond of lower Si)
- (f) Dangling bond in (d) or (e) is terminated by H

Defect density in our models: $\sim 10^{14}/\text{cm}^2$

Defect density in real devices: $\sim 10^{12}/\text{cm}^2$

Leakage Current



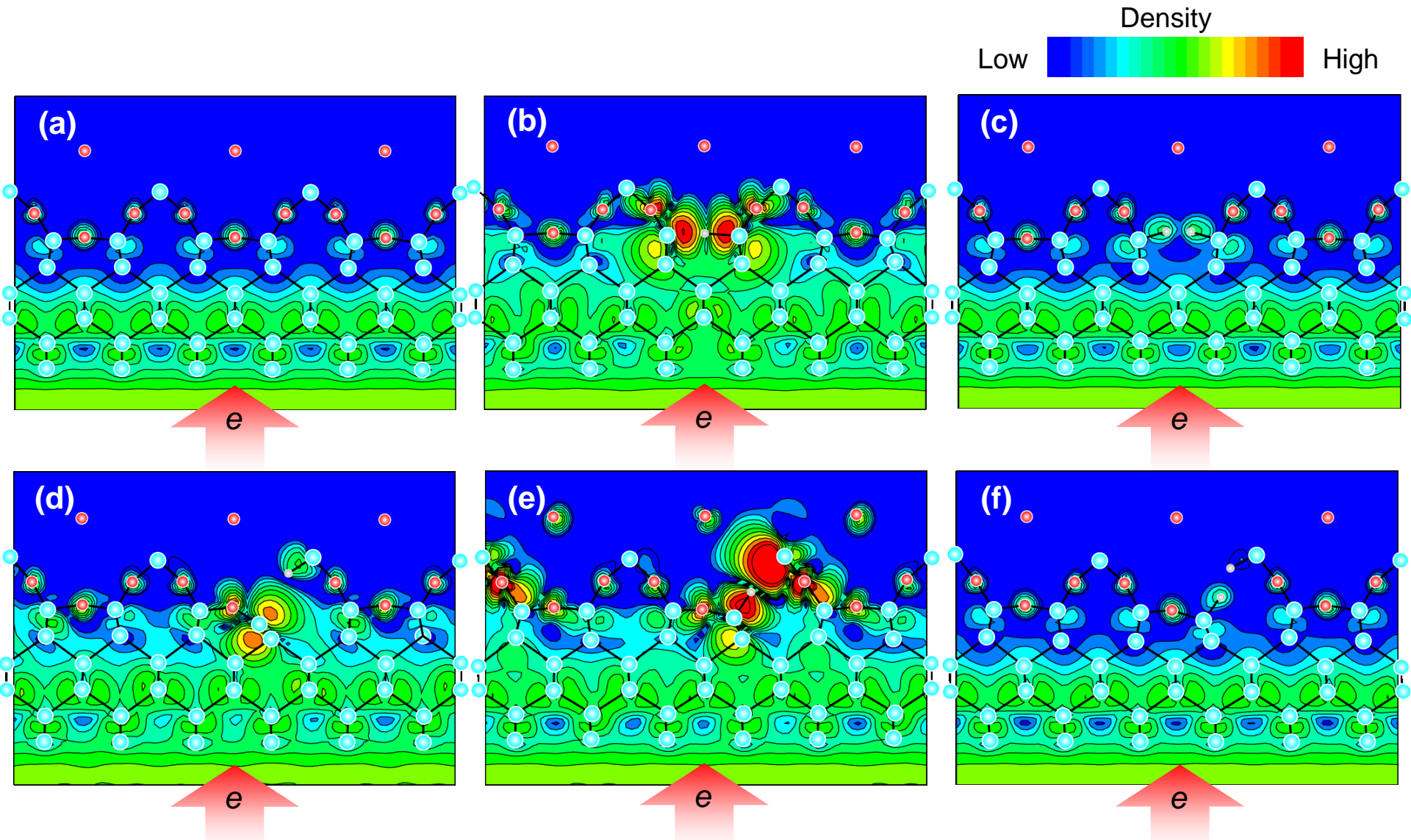
1 : 3.9 : 0.9 : 12.6 : 534 : 1.6
leakage current

● Si ● O ● H

The leakage current becomes high in the models with dangling bonds and low in the models where the dangling bonds are passivated.

The defects in the insulator film affects to leakage current larger than that at the interface.

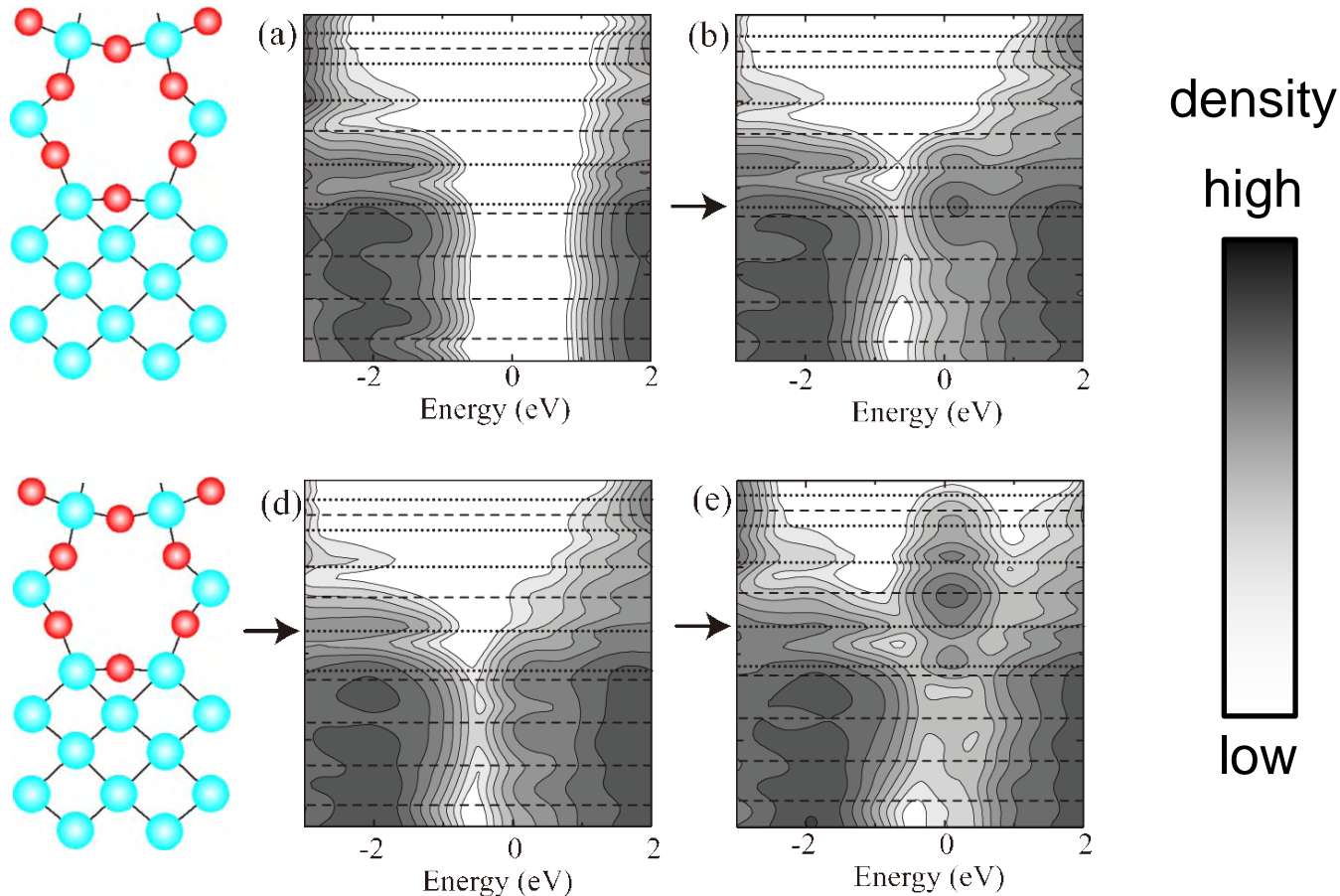
Charge Distributions of Scattering Waves from Lower Electrode



The incident electrons penetrate into insulator films via the defects.
The H atoms terminating dangling bonds play barriers for incident electrons to penetrate.

Local density of states at the interface

The density of states is integrated on plane parallel to interface as functions of relative energy from the Fermi energy.

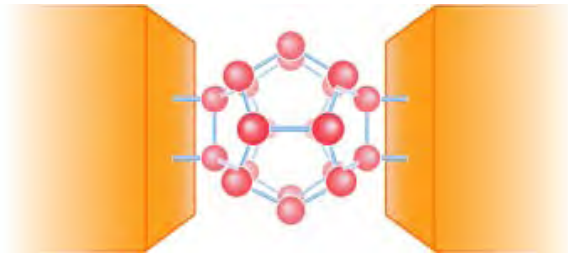


Transmission probability increases linearly with respect to the lateral width of the defect states, while it grows exponentially with respect to the vertical length.

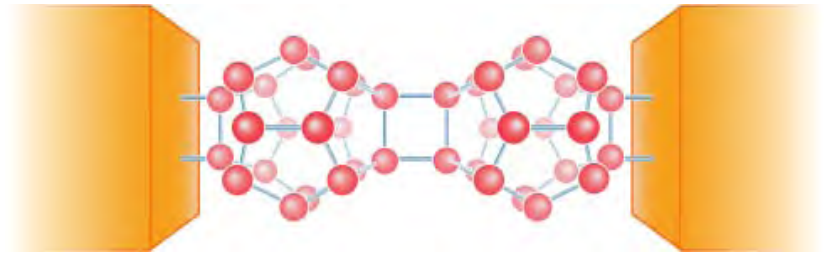
Electrons can penetrate easily because defect state of Model (e) extends vertically.

Example 4: Conductance of C_{20} wires

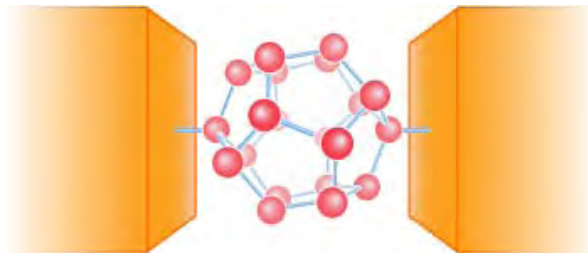
M. Otani, T. Ono and K. Hirose, Phys. Rev. B 69, 121408 (2004).



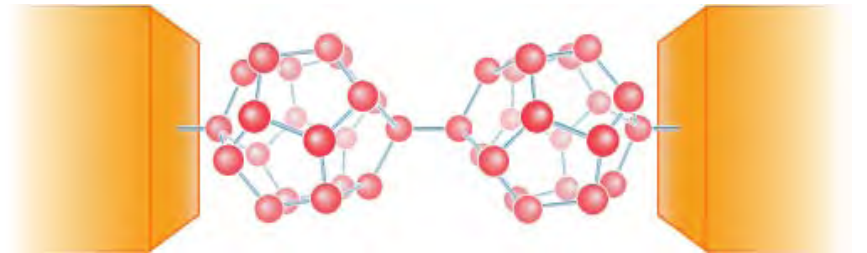
Double-bonded monomer



Double-bonded dimer



Single-bonded monomer



Single-bonded dimer

Computational conditions

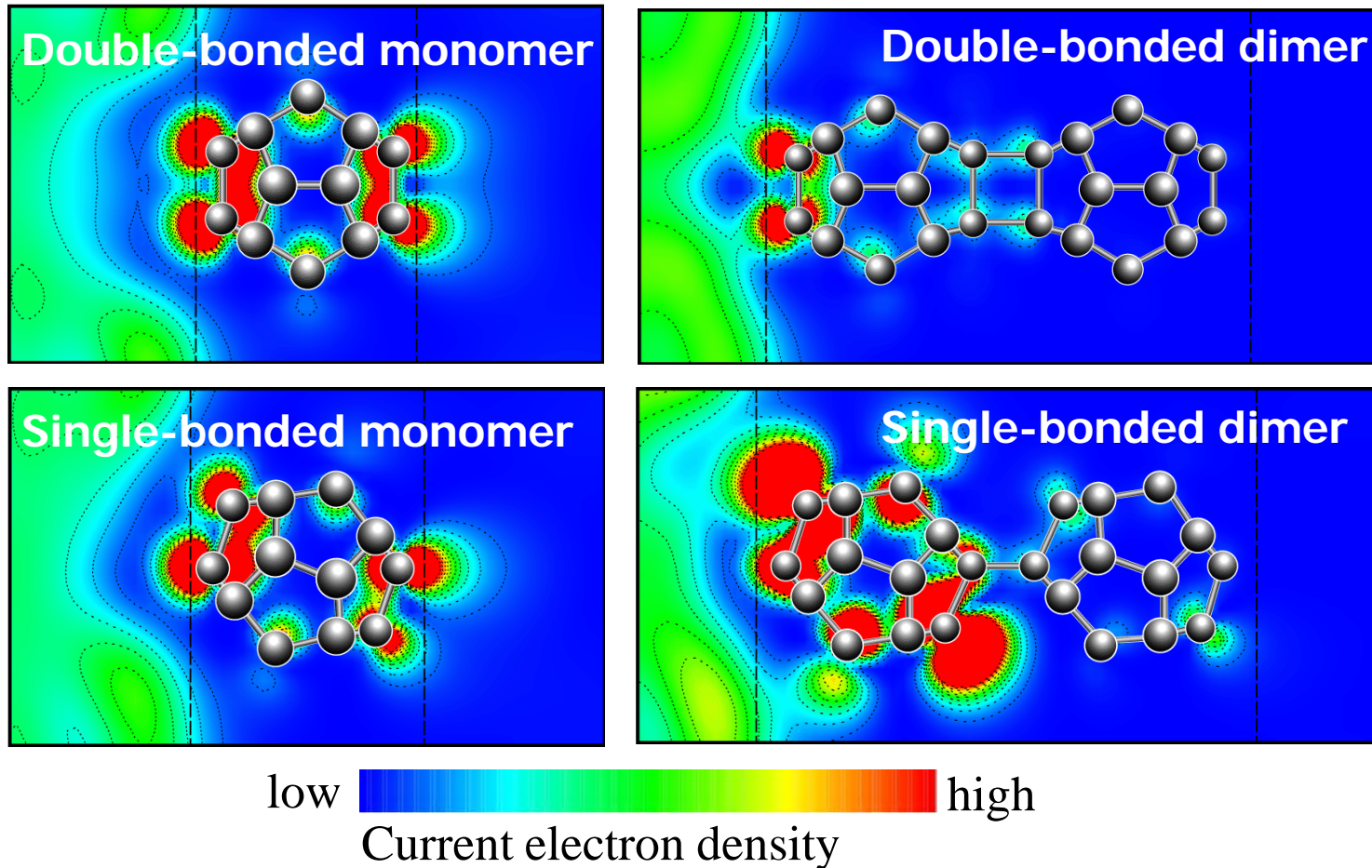
- Grid spacing 0.21 Å (Cutoff energy 61 Ry)
- Periodic boundary conditions are imposed at x and y directions. (The cell size is $L_x=11.43$ Å and $L_y=11.43$ Å.)
- The distance between jellium electrode and edge atom of the C_{20} chain 0.53 Å.
- Atoms of the C_{20} molecules are optimized by molecular-dynamics simulation.
- Norm conserving pseudopotential (NCPS97) is adopted.

Conductances and channel transmissions

(G ₀)	Monomer		Dimer	
	double	single	double	single
total	1.57	0.83	0.18	0.17
ch.1	0.47	0.36	0.16	0.07
ch.2	0.47	0.18	0.01	0.06
ch.3	0.35	0.17	0.00	0.03
ch.4	0.20	0.06	0.00	0.01

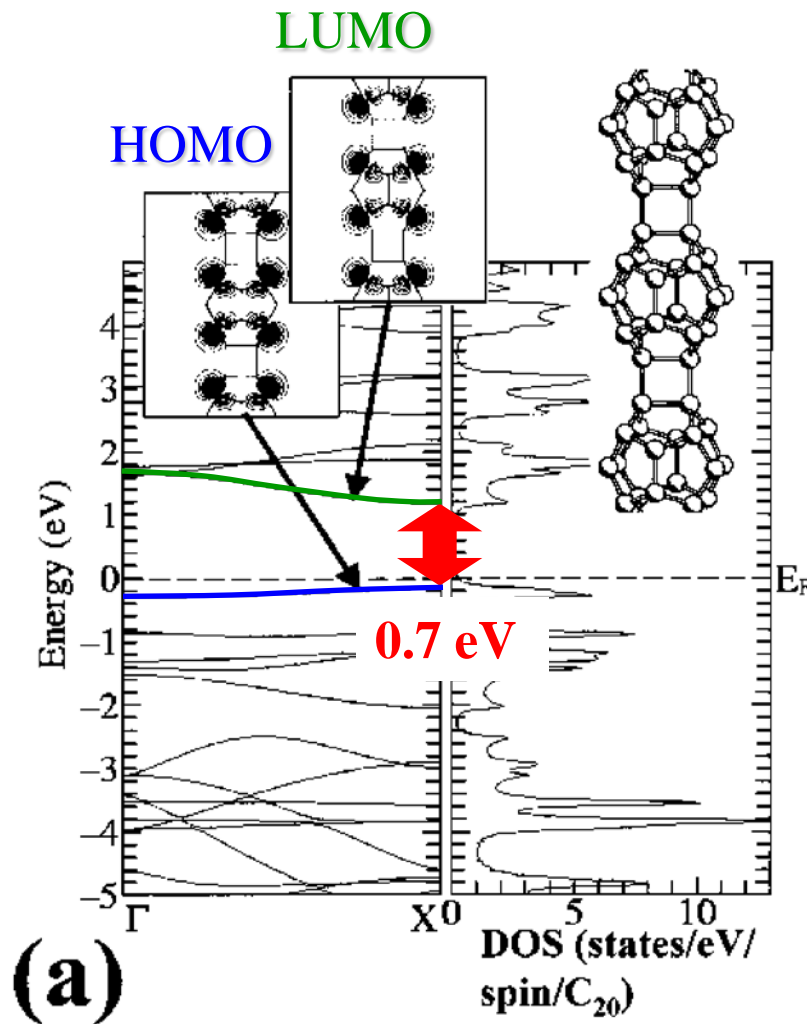
- The number of C₂₀ molecules between the electrodes largely affects the electron transport behavior.
- The difference in the conductance between the two monomer models is caused by the number of atoms facing the jellium electrodes.
- The higher conductance of the single-bonded dimer is consistent with the previous calculation that the band gap of an infinite single-bond chain is significantly smaller than that of a double-bonded one.

Charge distribution of the incident electron

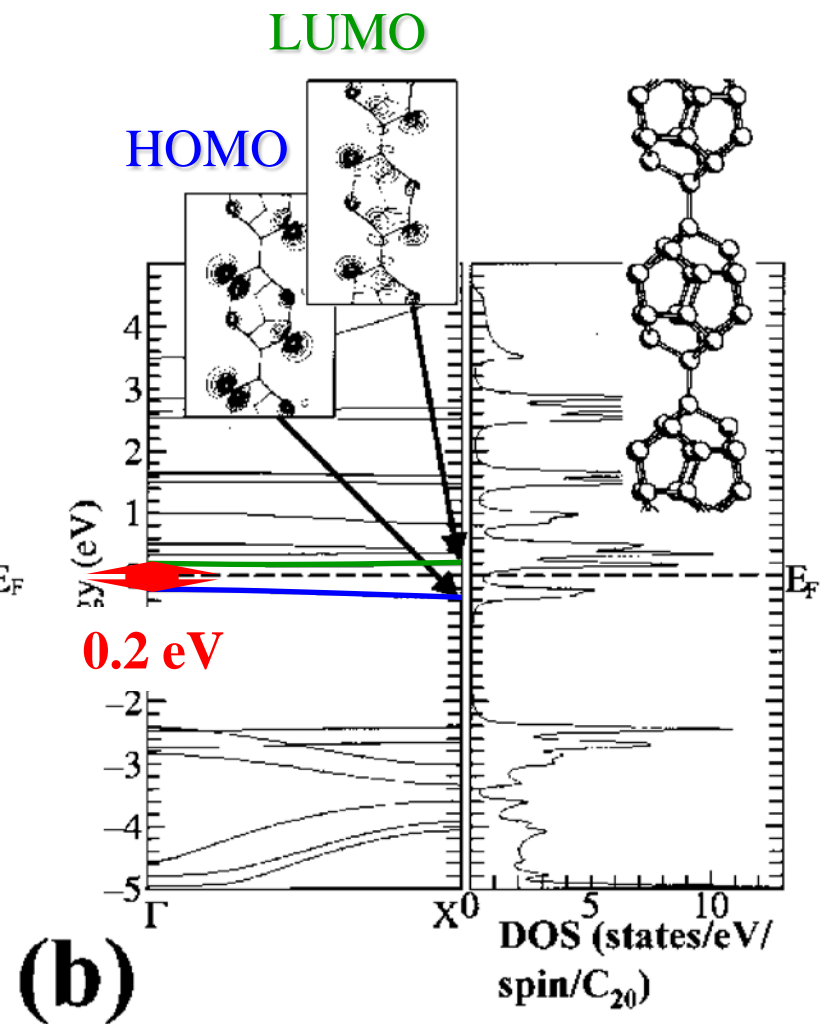


- Electron currents are found to pass along the C-C bonds, and not to directly cross through inside of the C₂₀ cages.
- Backscattering of incident electrons occurs at both the C₂₀-electrode interfaces and the C₂₀-C₂₀ junctions of the dimers, while reflection seldom takes place within the C₂₀ molecules.

Band structure of infinite wires



Double-bonded

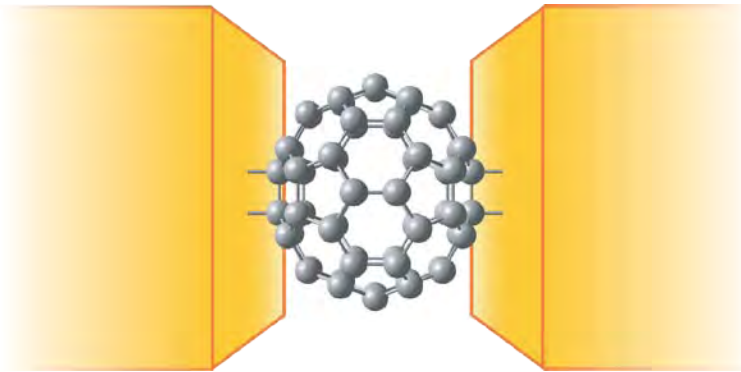


Single-bonded

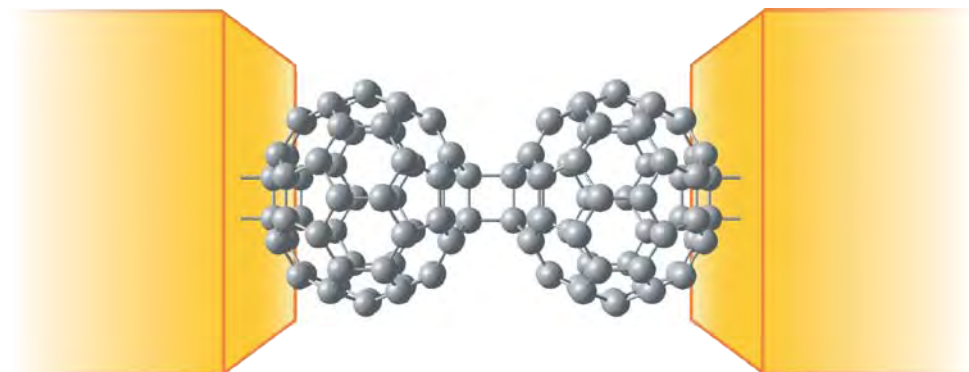
From Y. Miyamoto and M. Saito Phys. Rev. B **63** , R161401 (2001).

Example 5: Conductance of C_{60} wires

T. Ono and K. Hirose, Phys. Rev. Lett. 98, 026804, (2007).



monomer

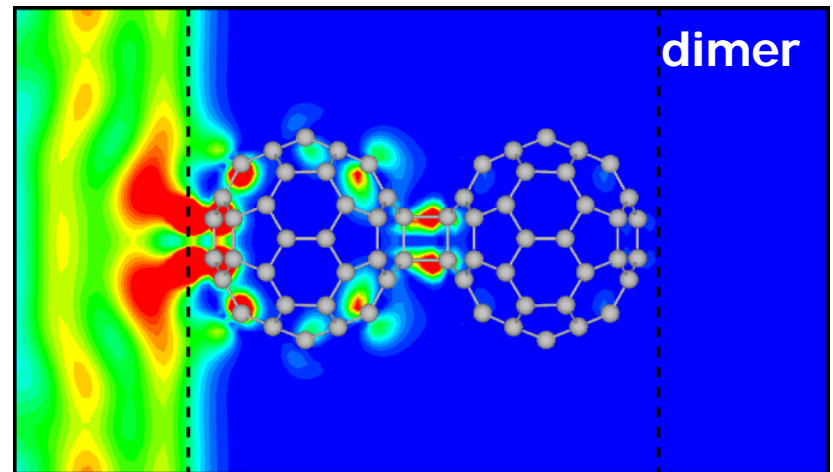
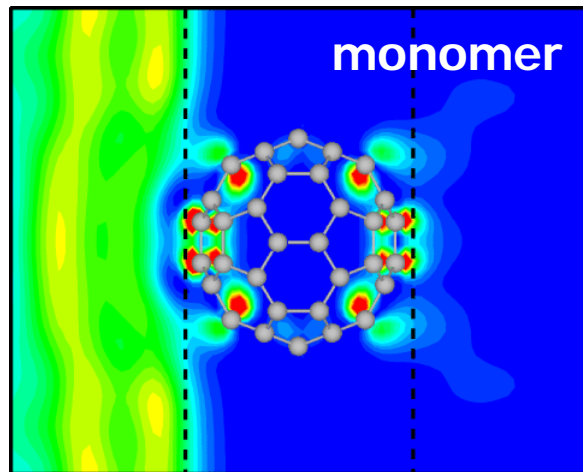


dimer

Computational conditions

- Grid spacing 0.26 Å (Cutoff energy 39 Ry)
- Periodic boundary conditions are imposed at x and y directions. (The cell size is $L_x=16.32$ Å and $L_y=16.32$ Å.)
- The distance between jellium electrode and edge atom of the C_{60} chain 0.53 Å.
- Atoms of the C_{60} molecules are optimized by molecular-dynamics simulation.
- Norm conserving pseudopotential (NCPS97) is adopted.

Charge distribution of the incident electron



Conductance

1.13 G_0

0.11 G_0

low  high
Current electron density

- Electron currents are found to pass along the C-C bonds, and not to directly cross through inside of the C₆₀ cages.
- Backscattering of incident electrons occurs at both the C₆₀-electrode interfaces and the C₆₀-C₆₀ junctions of the dimers, while reflection seldom takes place within the C₆₀ molecules.

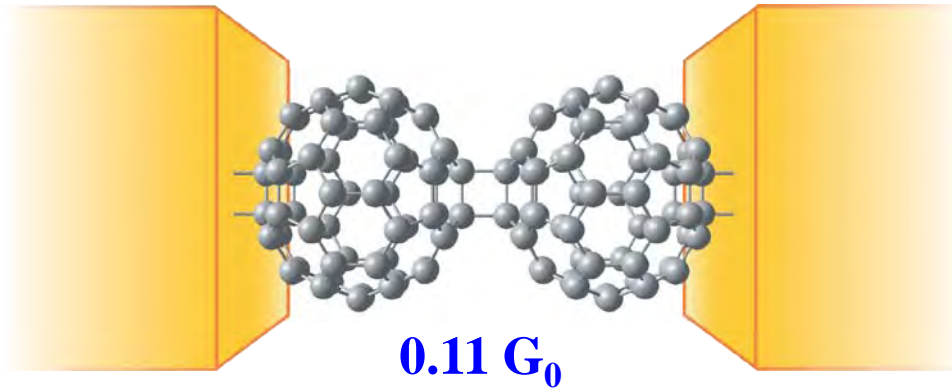
Situation is similar to that of C₂₀ chains!

Conductance of Li@C₆₀ chain

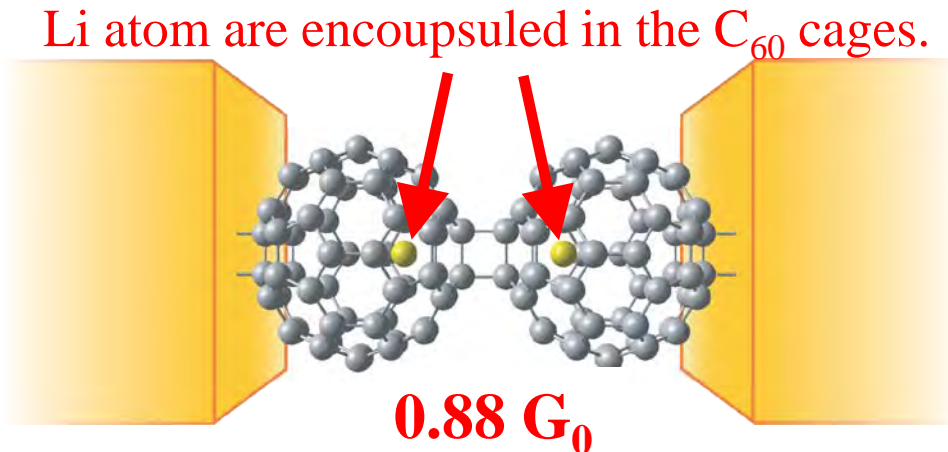
The conductance of C₆₀ dimer is quite low.

How much conductance of Li@C₆₀ dimer is?

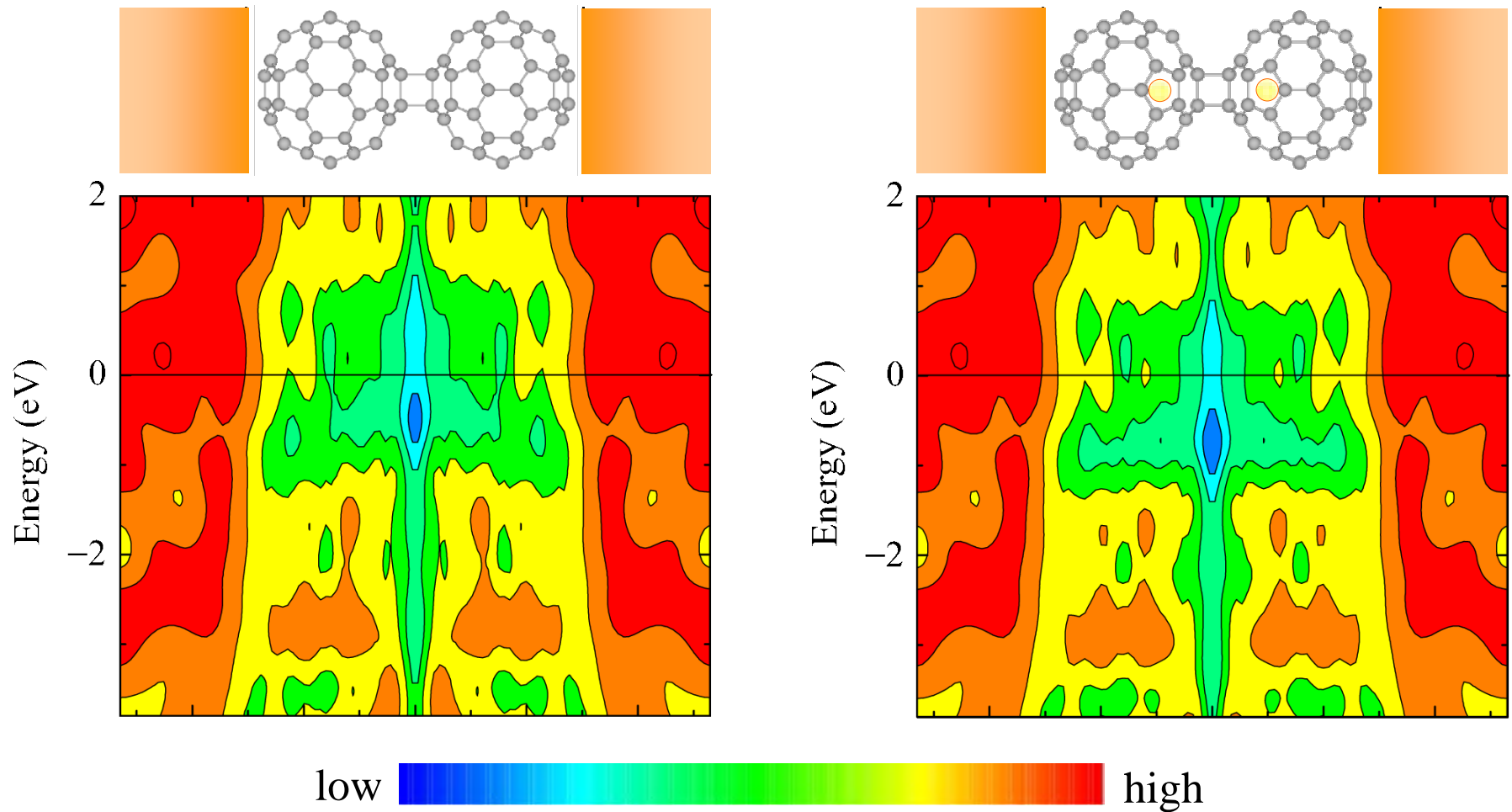
C₆₀ dimer



Li@C₆₀ dimer



Density of states in C₆₀ and Li@C₆₀ wires



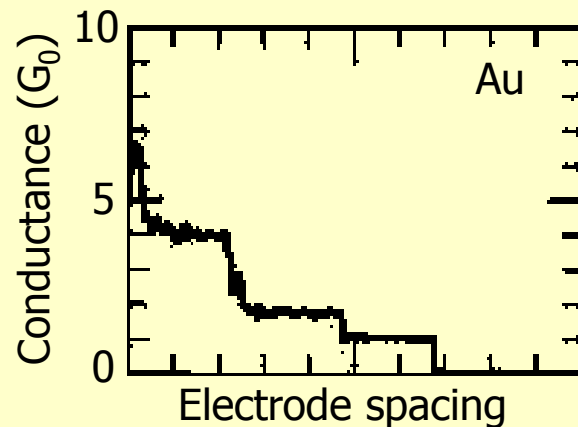
$$\text{density: } \rho(z, E) = \iint |\psi(r, E)|^2 dx dy$$

The DOS of the fullerene dimer at the Fermi level increases by inserting Li atom in the cage.

Example 6: Helical gold nanowire

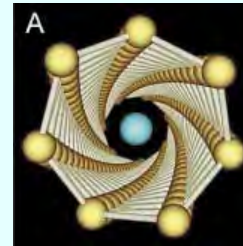
Experimental background

A single strand of gold atoms suspended between electrodes manifests conductance quantization in steps of $G_0 (=2e^2/h)$ as electrode spacing is increased.

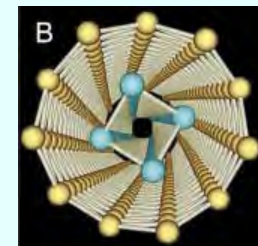


From Rubio *et al.*, PRL, **76**, 2302 (1996)

Recently, Takayanagi *et al.* found gold helical wires consisting of several atomic rows by TEM.



7-1 wire



11-4 wire

From Y. Kondo and K. Takayanagi, Science, **289**, 606 (2000)

- How high the conductances of these wires are?
- Where do electrons flow?

Synthesis and Characterization of Helical Multi-Shell Gold Nanowires

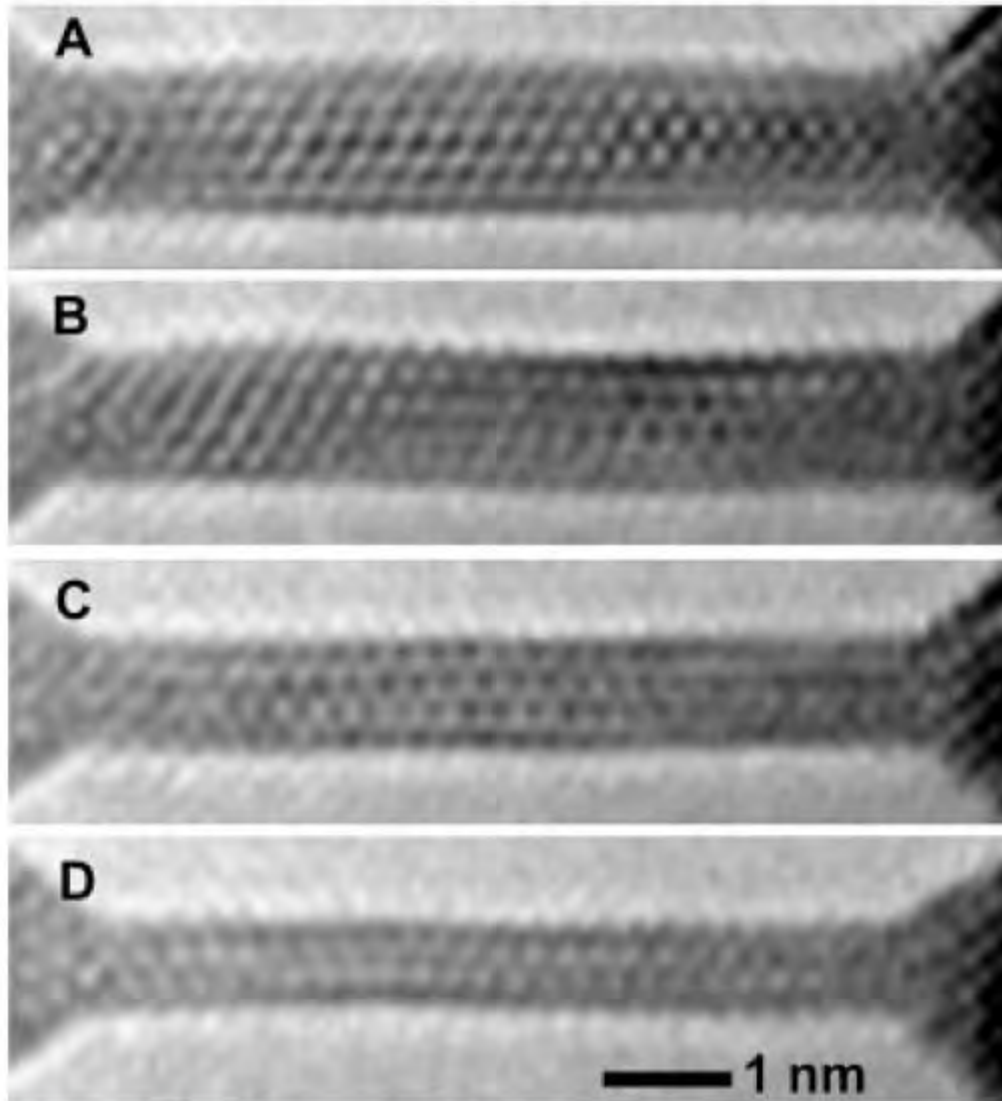


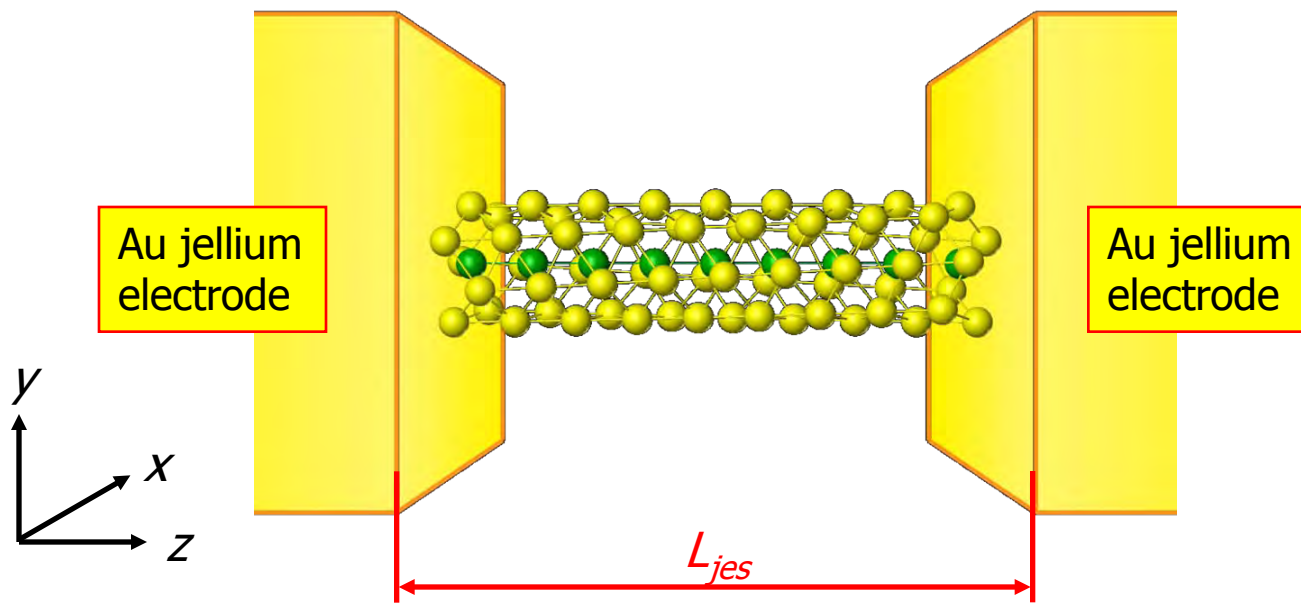
Fig. 1. TEM images of stable gold nanowires observed during one thinning process.

Y. Kondo and K. Takayanagi,
Science, **289**, 606 (2000)

Computational model

T. Ono and K. Hirose, Phys. Rev. Lett. **94**, 206806 (2005).

Au helical wire suspended between Au jellium electrodes



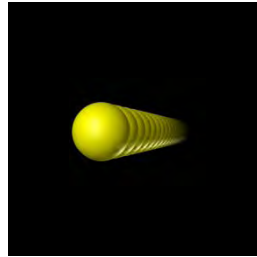
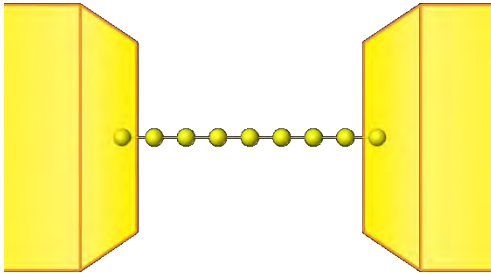
Computational conditions

- Grid spacing is 0.48 Å. (Cutoff energy 12 Ry)
- Periodic boundary conditions are imposed at x and y directions.
(The cell size is $L_x=21.2$ Å and $L_y=21.2$ Å.)
- Jellium electrode spacing is $L_{jes}=27.1$ Å.
(Equal to the electrode spacing 28.6 Å of Au(110) electrodes)
- Gold atoms are treated by the local pseudopotential.
(Only 6s electrons are considered.)

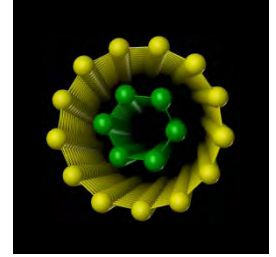
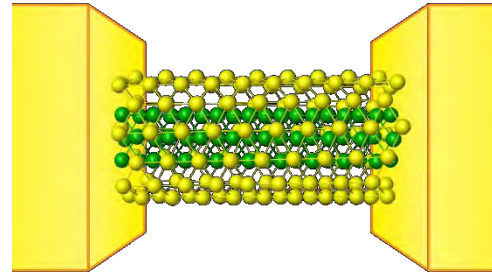
Computational model

Several helical wires are inserted between electrodes.

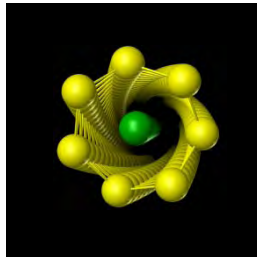
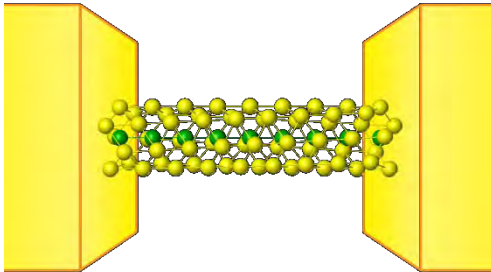
Single-row wire



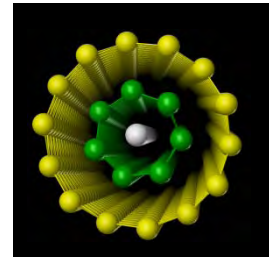
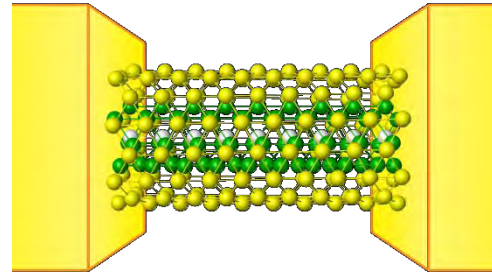
13-6 wire



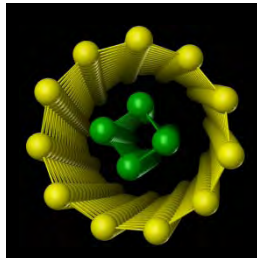
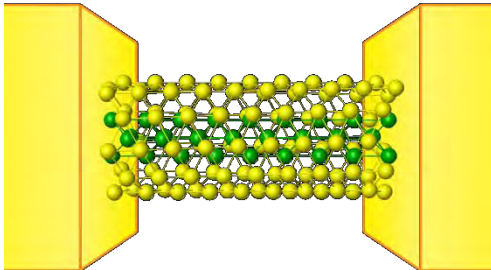
7-1 wire



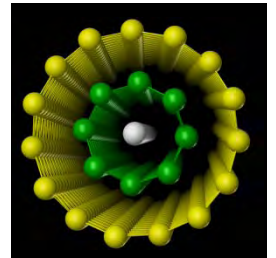
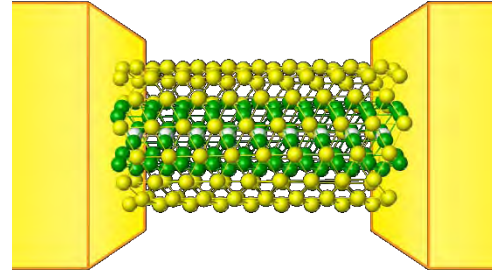
14-7-1 wire



11-4 wire



15-8-1 wire



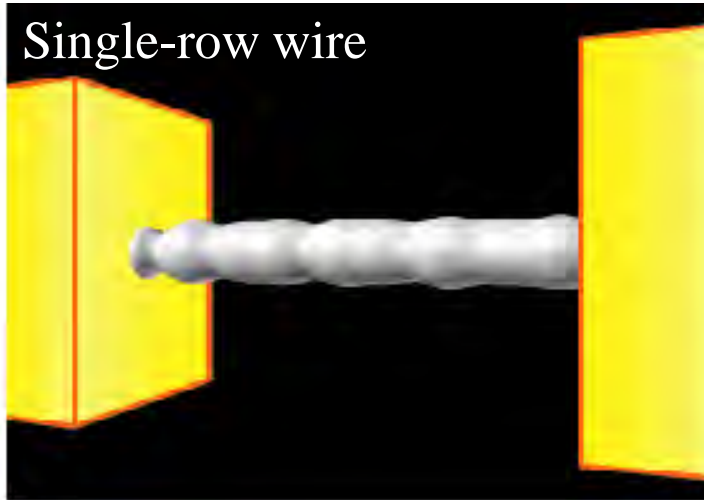
Conductances and channel transmissions

	Single-row wire	7-1 wire	11-4 wire	13-6 wire	14-7-1 wire	15-8-1 wire
Conductance	0.96G₀	5.19 G₀	9.08 G₀	11.97 G₀	13.82 G₀	14.44 G₀
1 st ch	0.958	0.997	1.000	0.996	1.000	1.000
2 nd ch	---	0.995	0.991	0.992	0.999	0.996
3 rd ch	---	0.970	0.986	0.982	0.991	0.991
4 th ch	---	0.938	0.890	0.978	0.984	0.982
5 th ch	---	0.653	0.884	0.962	0.959	0.975
6 th ch	---	0.640	0.874	0.958	0.947	0.954
7 th ch	---	---	0.753	0.940	0.94	0.942
8 th ch	---	---	0.748	0.878	0.927	0.931
9 th ch	---	---	0.620	0.872	0.893	0.899
10 th ch	---	---	0.517	0.744	0.888	0.891
11 th ch	---	---	0.497	0.735	0.881	0.841
12 th ch	---	---	0.318	0.706	0.867	0.834
13 th ch	---	---	---	0.618	0.770	0.732
14 th ch	---	---	---	0.383	0.700	0.691
15 th ch	---	---	---	0.200	0.542	0.645
16 th ch	---	---	---	0.002	0.527	0.595
17 th ch	---	---	---	---	---	0.537

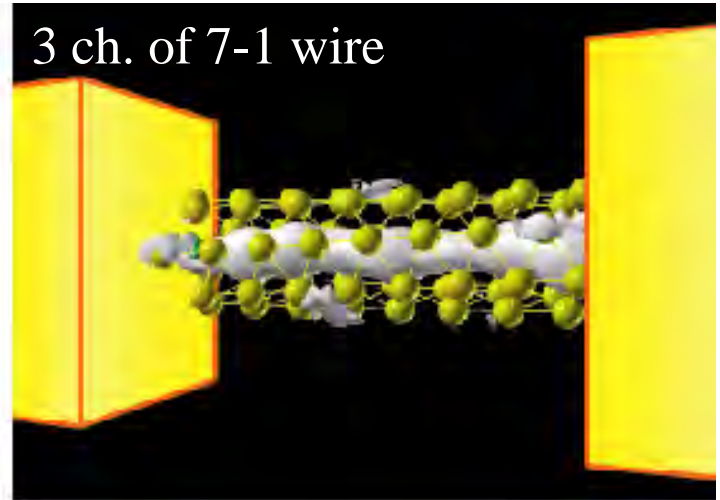
- The number of conduction channels in the single-row nanowire is one and the conductance is 1 G₀.
- The number of conduction channels in the nanowires does not correspond with the number of atom rows forming the HGNs.

Current charge distribution in Au nanowire

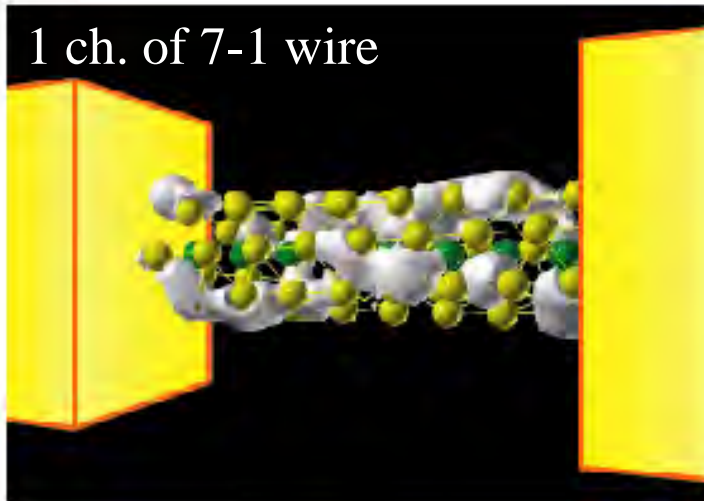
(a) Single-row wire



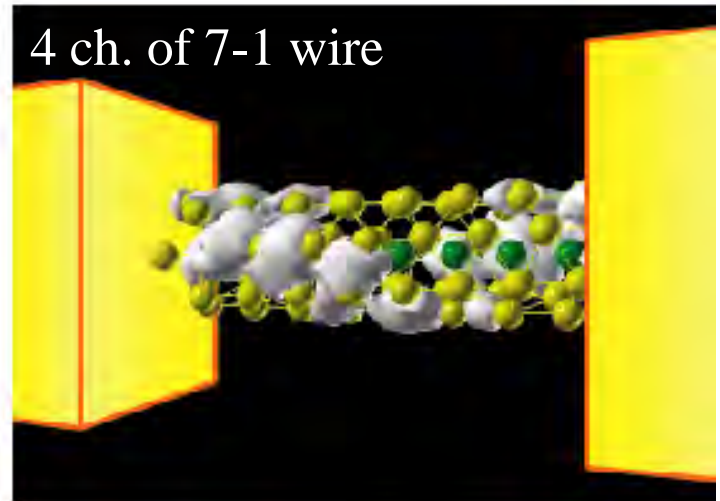
(c) 3 ch. of 7-1 wire



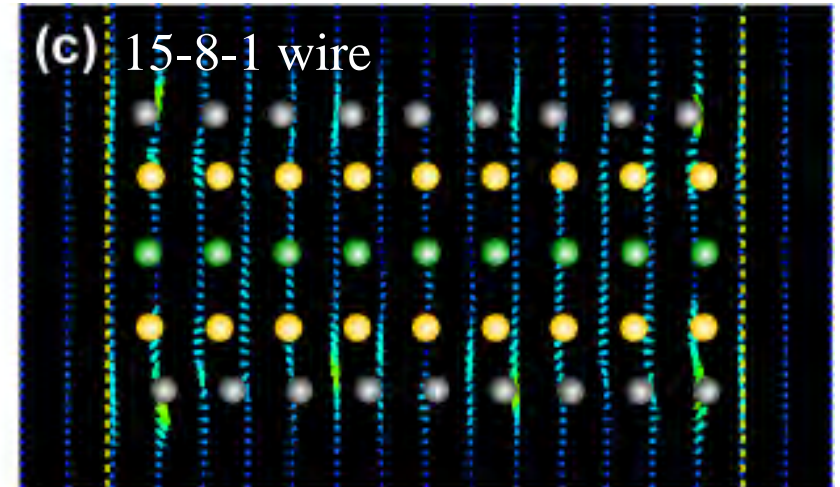
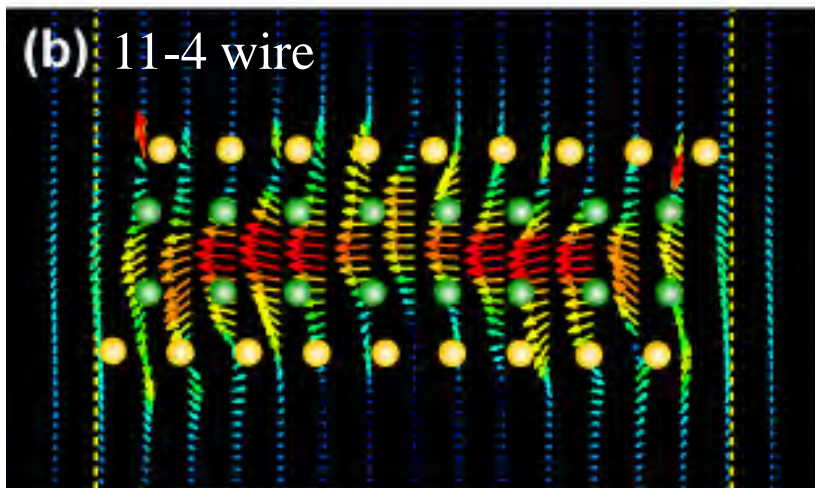
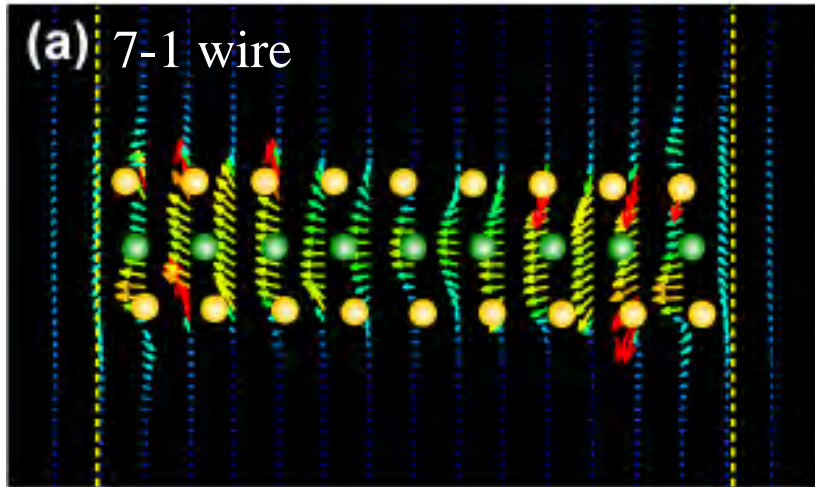
(b) 1 ch. of 7-1 wire




(d) 4 ch. of 7-1 wire



Magnetic field induced by the current



Magnetic flux density per bias voltage (T/mV)



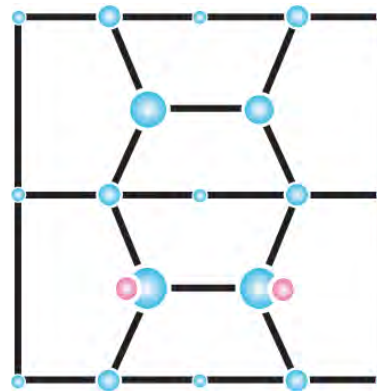
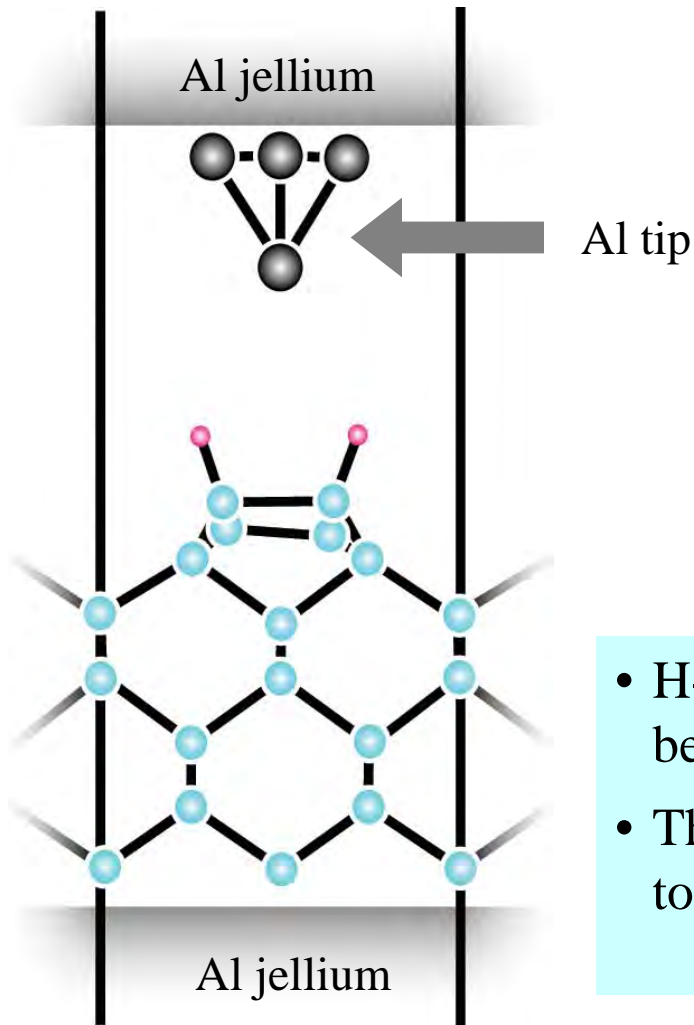
0 0.008




Example 7: Tunnel current in STM

T. Ono, S. Horie, K. Endo and K Hirose, Phys. Rev. B 73, 245314 (2006).

Side view

Top view

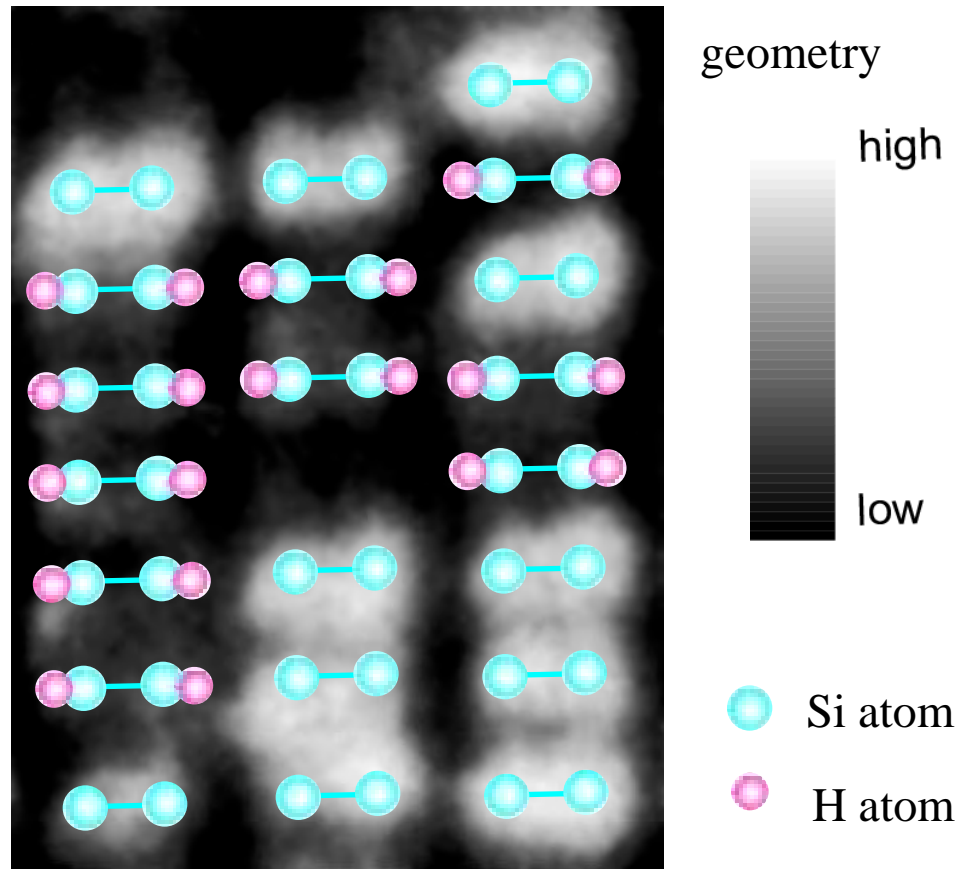


-  Si atom
-  H atom
-  Al atom

- H-adsorbed Si(001) and Al tip are suspended between semi-infinite Al jellium electrodes.
- The distance between the edge of the tip and the top-most Si atom of the surface is set to be $\sim 5 \text{ \AA}$.

STM image of H-adsorbed Si(001)

Experimental background



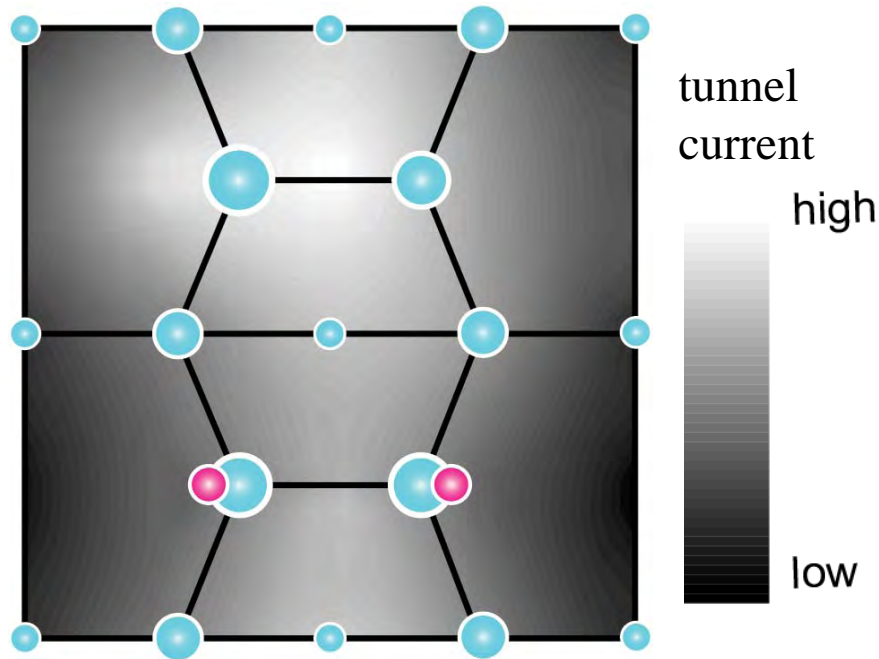
From Y. Wang *et al.*, J. Vac. Sci. Tech. A, **12**, 2051 (1994)

H-adsorbed dimers are observed to be geometrically **lower** than bare dimers in the topographic image, although the H atoms locate **above** the bare dimers.

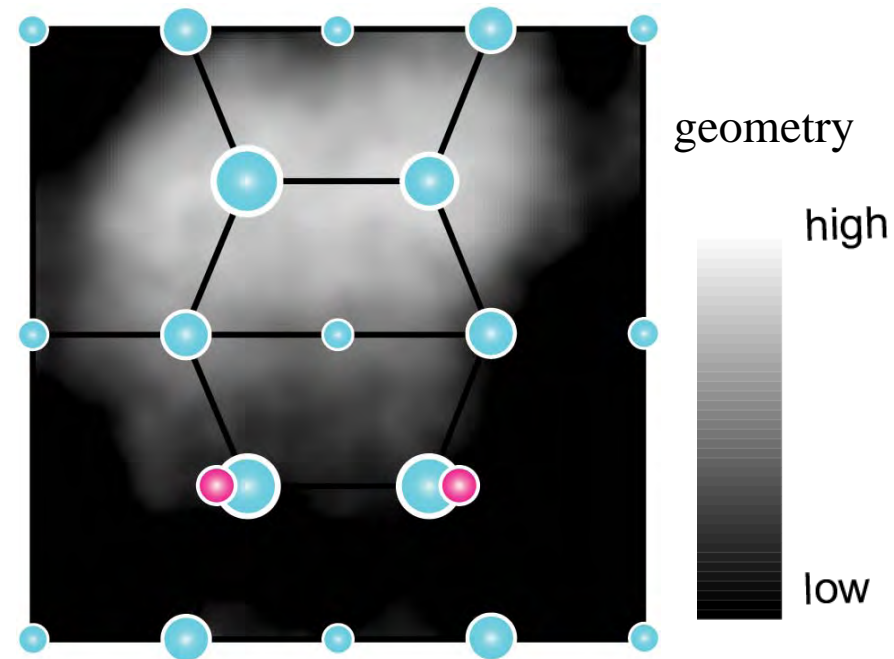
STM image of Si(001) surface

T. Ono, S. Horie, K. Endo and K Hirose, Phys. Rev. B 73, 245314 (2006).

Theoretical result
(Current image)



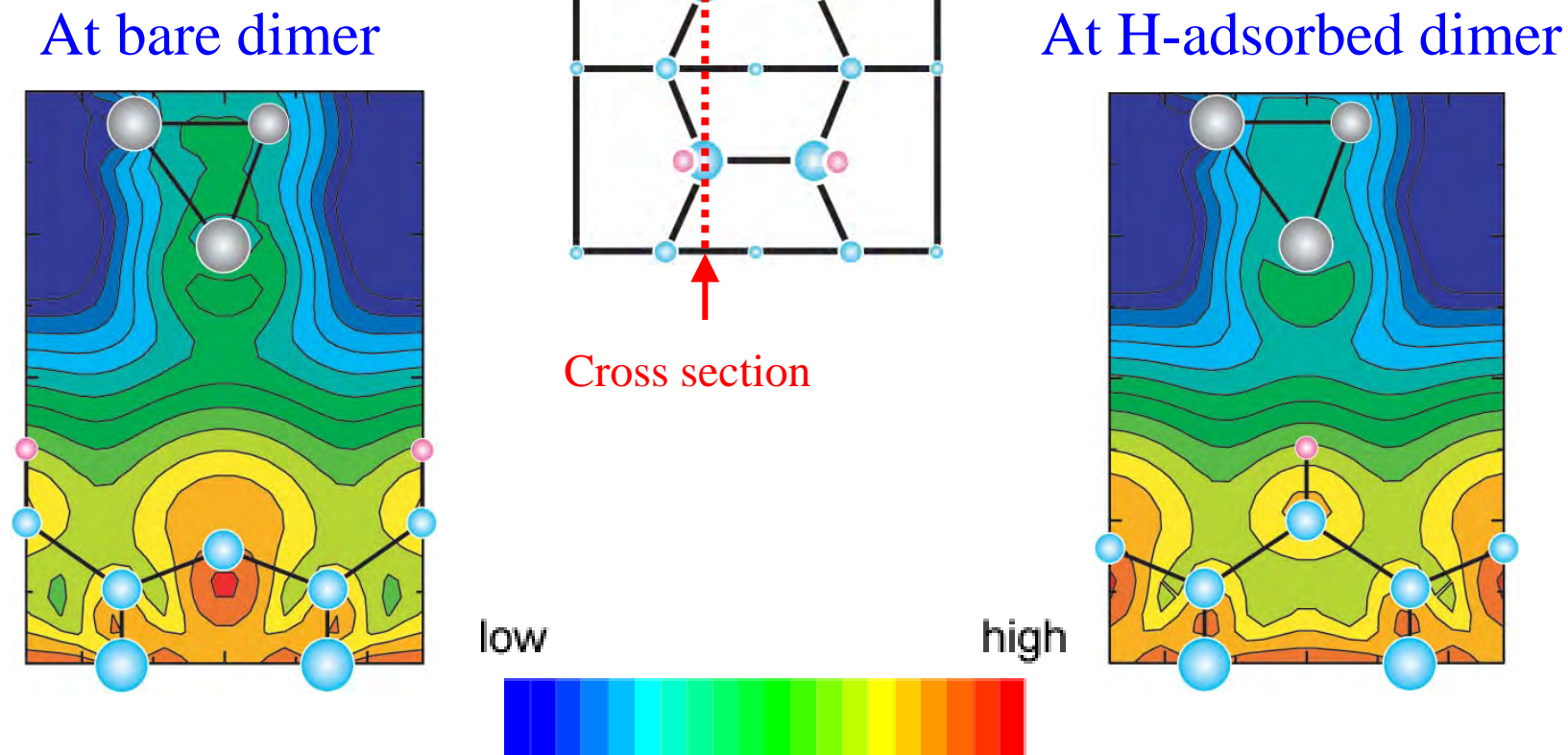
Experimental result
(Topographic image)



Y. Wang *et al.*, J. Vac. Sci. Tech. A, **12**, 2051 (1994).

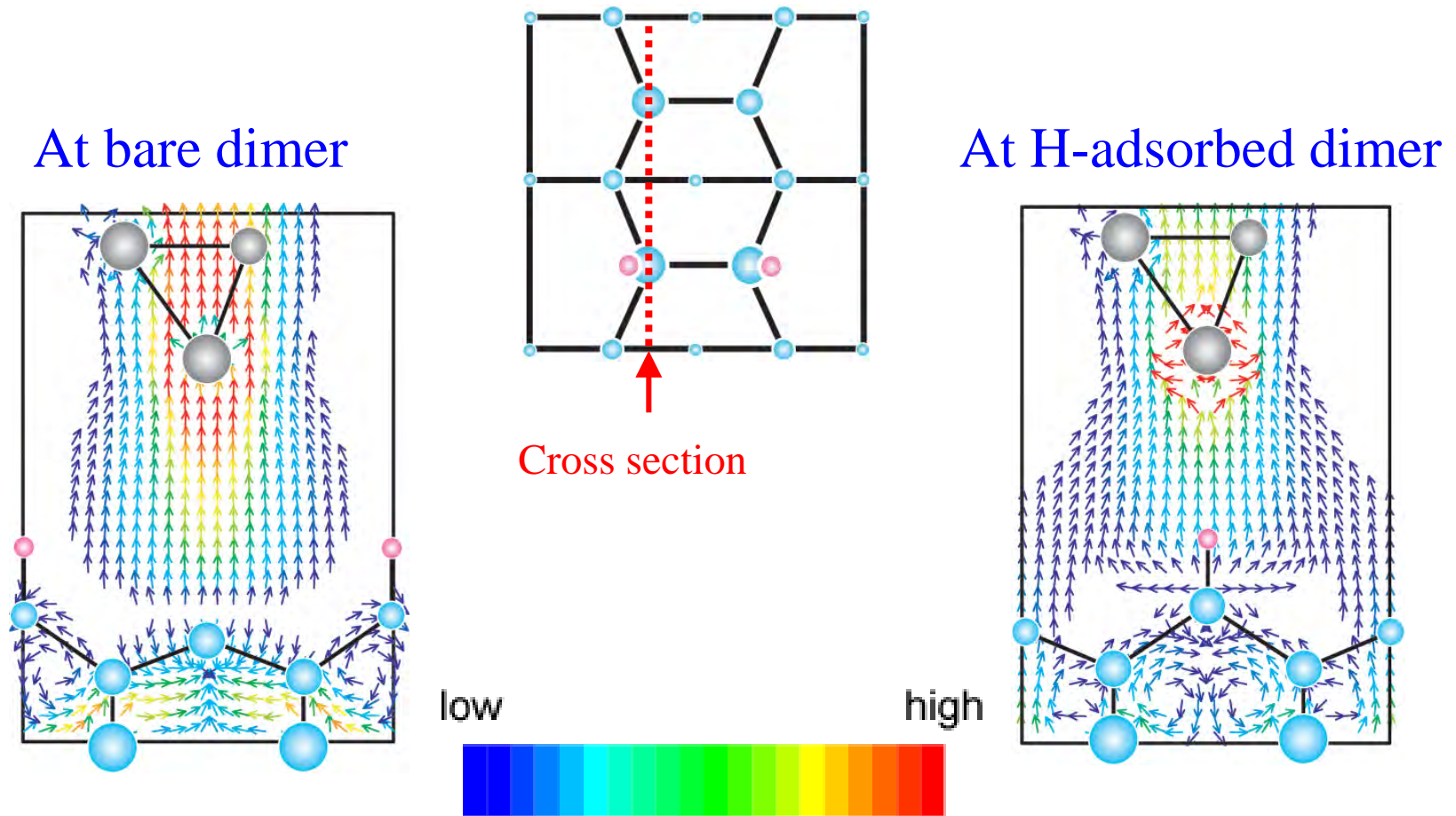
Since the tip must approach closer to the sample surface in order to achieve the constant tunnel current, the H-adsorbed dimer looks geometrically lower than the bare dimer in the STM, which agrees with the experimental results

Tunnel current charge distributions



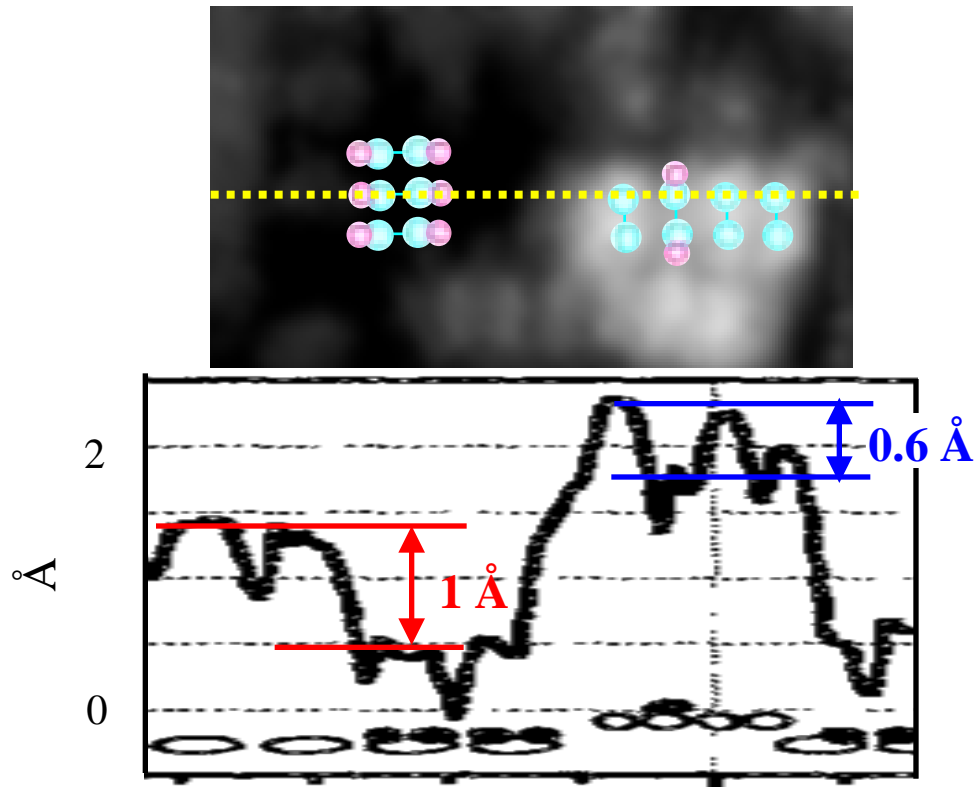
- The π states of bare dimer affect the tunnel current.
- Certain amount of charge is observed around the H-adsorbed dimer.

Tunnel current distributions



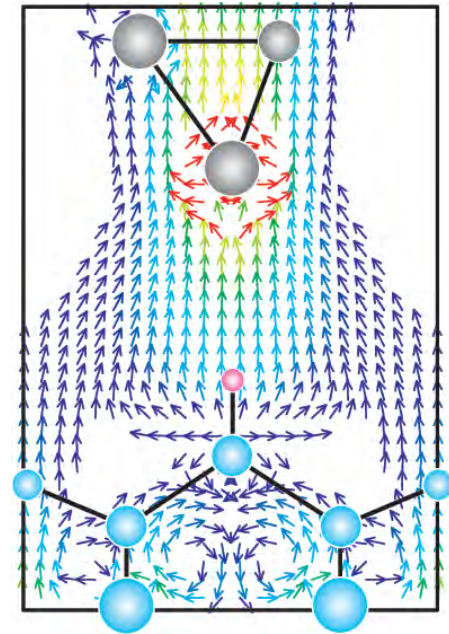
- Although certain amount of charge distributions is observed around the hydrogen adsorbed dimer, the current distribution around the dimer is small.
- There is certain contribution from the π bonding state to the tunnel current even when the tip locates above the hydrogen adsorbed dimer.

STM image of H-adsorbed Si(001)



Y. Wang *et al.*, J. Vac. Sci. Tech. A, **12**, 2051 (1994).

At H-adsorbed dimer



The contribution of the p state of the adjacent bare dimer leads the STM image where the H-adsorbed dimer neighboring to the bare dimer appears geometrically higher than those sandwiched between H-adsorbed dimers in the [010] direction.

Thank you for your attention!!